

A finite element formulation for incompressible viscous flow based on the principle of minimum pressure gradient

Julian J. Rimoli

Department of Mechanical and Aerospace Engineering, University of California, Irvine, CA 92697, USA

jrimoli@uci.edu

Abstract

We present a finite element formulation for incompressible viscous flow based on the principle of minimum pressure gradient (PMPG). This variational principle, recently established by Taha, Gonzalez & Shorbagy (*Phys. Fluids*, vol. 35, 2023), states that the Navier–Stokes equations are equivalent to determining the rate of change $\partial_t \mathbf{v}$ at each instant by minimizing the L^2 norm of the implied pressure gradient, subject to incompressibility and boundary conditions. We discretize the PMPG functional directly using Q9 biquadratic finite elements and minimize over the nodal velocity rates (Rayleigh–Ritz). No pressure degrees of freedom appear; incompressibility and boundary conditions are enforced as linear equality constraints through a monolithic saddle-point system, whose Lagrange multipliers provide wall forces without pressure reconstruction. We verify the formulation against exact Poiseuille flow (machine-precision recovery) and the Kovasznay solution (convergence rate ~ 3.3), and validate it against published benchmarks for the lid-driven cavity, the backward-facing step, and flow past a circular cylinder. The formulation produces smooth, oscillation-free solutions on coarse meshes in the convection-dominated regime without stabilization. We further show that the element-wise PMPG functional density serves as a built-in error indicator for adaptive mesh refinement, and that the stationarity condition can be read backwards to estimate the kinematic viscosity directly from velocity field measurements.

Keywords: finite elements, incompressible viscous flow, principle of minimum pressure gradient, Rayleigh–Ritz method, velocity-only formulation, error estimation

1 Introduction

1.1 The principle of minimum pressure gradient

The numerical simulation of incompressible viscous flow has been a central topic in computational mechanics for over half a century. The prevailing approaches (finite element, finite volume, and spectral methods) discretize the Navier–Stokes equations directly, treating the

pressure either as a primary unknown (mixed methods) or through projection/fractional-step algorithms [1, 2, 3]. In mixed formulations, the velocity–pressure pair must satisfy the Babuška–Brezzi inf-sup condition [4, 5] to ensure stability, which constrains the choice of interpolation spaces. Projection methods decouple velocity and pressure through operator splitting, but can introduce a splitting error that compromises accuracy at steady state [3].

A fundamentally different perspective was recently established by Taha, Gonzalez & Shorbagy [6], who proved that the incompressible Navier–Stokes equations are equivalent to a constrained optimization problem: at each instant in time, the rate of change $\partial_t \mathbf{v}$ is determined by minimizing the L^2 norm of the implied pressure gradient over the domain, subject to incompressibility and boundary conditions. This is the *principle of minimum pressure gradient* (PMPG). The principle has deep roots in classical analytical mechanics (Gauss’s principle of least constraint [7] and Appell’s formulation [8]), first extended to ideal flows by Gonzalez & Taha [9] and subsequently generalized to viscous flows [6].

The PMPG principle recasts the Navier–Stokes equations as a constrained minimization rather than a boundary-value problem, calling for a fundamentally different discretization strategy: rather than writing the weak form and applying Galerkin projection, one can substitute a finite-dimensional velocity approximation directly into the PMPG functional and minimize over the nodal velocity rates (the classical Rayleigh–Ritz approach), with constraints enforced exactly through Lagrange multipliers. Demonstrations of this principle in [6, 9], however, relied on analytical or semi-analytical velocity representations, limiting their applicability to simple geometries. A general-purpose implementation requires a finite element discretization capable of handling arbitrary domains and boundary conditions; this is the subject of the present work.

1.2 Objectives and contributions

The goal of this work is to develop a general-purpose finite element implementation of the PMPG principle for viscous incompressible flow. We make five contributions:

1. **First FEM implementation of PMPG for viscous flow.** We apply the Rayleigh–Ritz method to the PMPG functional: the Q9 biquadratic velocity interpolation is substituted into the variational principle, converting it into a finite-dimensional constrained minimization over the nodal velocity rates. The resulting solver handles general two-dimensional geometries with no-slip walls, prescribed inlet profiles, and free-outflow boundaries.
2. **Velocity(rate)-only primal formulation.** No pressure FE space is introduced and no inf–sup velocity–pressure pairing is required. Pressure-related quantities enter through the dual variables (Lagrange multipliers) associated with the imposed incompressibility and boundary constraints, enabling force extraction without pressure reconstruction.
3. **Monolithic constraint-based architecture.** Divergence-free flow and all boundary conditions are encoded as linear equality constraints and enforced through a monolithic saddle-point system at each time step. Unlike projection methods, which introduce splitting errors between the viscous and incompressibility sub-problems, the monolithic

approach enforces all constraints simultaneously and converges to the exact steady state at machine precision for problems whose solutions lie in the finite element space. Because convection enters only through the explicit right-hand side, the system matrix is symmetric positive definite regardless of the Reynolds number, and the formulation produces oscillation-free solutions without stabilization even on coarse meshes in the convection-dominated regime.

4. **Built-in error indicator and adaptive refinement.** The element-wise PMPG functional density measures the local momentum residual and serves as a zero-cost error indicator: no adjoint problem, reference mesh, or additional solve is needed. We demonstrate its use for adaptive mesh refinement on the backward-facing step.
5. **Inverse viscosity estimation from velocity data.** We show that the PMPG stationarity condition can be read backwards to recover the kinematic viscosity directly from velocity field measurements (e.g., PIV data). The constraint forces are eliminated by projecting onto the divergence-free subspace, and the viscosity is obtained from a single ratio of inner products, requiring no forward solve, pressure reconstruction, or iterative optimization.

1.3 Outline

The remainder of this paper is organized as follows. Section 2 develops the PMPG formulation: the Rayleigh–Ritz discretization of the variational principle, the Q9 finite element interpolation, the divergence-free constraint, boundary conditions, the monolithic saddle-point solver, adaptive Courant–Friedrichs–Lewy (CFL) time stepping, and the extraction of wall forces from Lagrange multipliers. Section 3 presents verification against the exact Poiseuille and Kovasznay solutions. Section 4 validates the method against published benchmark data for the lid-driven cavity, the backward-facing step, and flow past a circular cylinder. Section 5 shows that the element-wise PMPG functional provides a natural error indicator and demonstrates its use for adaptive mesh refinement. Section 6 develops the inverse viscosity estimation method and demonstrates it on synthetic PIV data. Section 7 summarizes the contributions and discusses future directions.

2 Formulation

2.1 The PMPG variational principle

Consider incompressible viscous flow of a Newtonian fluid with constant density $\rho = 1$ and kinematic viscosity ν in a domain $\Omega \subset \mathbb{R}^2$. The velocity field $\mathbf{v}(\mathbf{x}, t)$ satisfies the Navier–Stokes equations:

$$\frac{\partial \mathbf{v}}{\partial t} + (\mathbf{v} \cdot \nabla) \mathbf{v} = -\nabla p + \nu \nabla^2 \mathbf{v} \quad \text{in } \Omega, \quad (1)$$

$$\nabla \cdot \mathbf{v} = 0 \quad \text{in } \Omega, \quad (2)$$

with boundary conditions on $\partial\Omega$.

Taha et al. [6] proved that the solution of (1)–(2) can be equivalently characterized through a minimization principle. The PMPG principle states that, at each instant, the time derivative $\partial_t \mathbf{v}$ is the one that minimizes the L^2 norm of the implied pressure gradient:

$$\min_{\partial_t \mathbf{v}} \mathcal{J}(\partial_t \mathbf{v}) = \frac{1}{2} \int_{\Omega} \left| \frac{\partial \mathbf{v}}{\partial t} + (\mathbf{v} \cdot \nabla) \mathbf{v} - \nu \nabla^2 \mathbf{v} \right|^2 d\Omega, \quad (3)$$

for all velocity fields that satisfy $\nabla \cdot \mathbf{v} = 0$ and Dirichlet boundary conditions. In this formulation, the current velocity \mathbf{v} and its spatial derivatives are known at a given instant of time; the unknown is $\partial_t \mathbf{v}$, which appears as the first term in the integrand. The functional is therefore quadratic in $\partial_t \mathbf{v}$, and its minimization subject to the aforementioned constraints.

The quadratic structure of the PMPG functional is the key property that makes it attractive to finite element discretization. Just as the minimum potential energy principle in linear elasticity (quadratic in displacements) leads via Rayleigh–Ritz to symmetric linear systems that form the basis of structural finite element methods, the PMPG functional (quadratic in $\partial_t \mathbf{v}$) should yield a symmetric linear system when discretized with finite element shape functions. The next section develops this discretization.

2.2 Rayleigh–Ritz discretization

We discretize the velocity field using finite element shape functions $N_a(\mathbf{x})$, writing $\mathbf{v}(\mathbf{x}, t) = \sum_a N_a(\mathbf{x}) \mathbf{d}_a(t)$, where $\mathbf{d} \in \mathbb{R}^{n_{\text{dofs}}}$ collects the nodal velocity coefficients. The time derivative (the field with respect to which the minimization is carried out) is interpolated with the same basis: $\partial_t \mathbf{v} = \sum_a N_a \dot{\mathbf{d}}_a$. The specific choice of element and shape functions is deferred to Section 2.3; the development here is independent of that choice.

Substituting into the PMPG functional (3) converts the infinite-dimensional minimization into a finite-dimensional quadratic program over $\dot{\mathbf{d}}$. Denoting the residual vector

$$\mathbf{R}(\dot{\mathbf{d}}) = \frac{\partial \mathbf{v}}{\partial t} + (\mathbf{v} \cdot \nabla) \mathbf{v} - \nu \nabla^2 \mathbf{v} = \sum_a N_a \dot{\mathbf{d}}_a + \mathbf{g}, \quad (4)$$

where $\mathbf{g} = (\mathbf{v} \cdot \nabla) \mathbf{v} - \nu \nabla^2 \mathbf{v}$ collects the terms that depend on the known velocity field, the functional becomes $\mathcal{J} = \frac{1}{2} \int_{\Omega} |\mathbf{R}|^2 d\Omega$, which is quadratic in $\dot{\mathbf{d}}$ with a unique minimum. Differentiating with respect to \dot{d}_i (the DOF associated with component k at node a) gives

$$\frac{\partial \mathcal{J}}{\partial \dot{d}_i} = \int_{\Omega} \mathbf{R} \cdot \frac{\partial \mathbf{R}}{\partial \dot{d}_i} d\Omega = \int_{\Omega} R_k N_a d\Omega = 0. \quad (5)$$

Expanding $R_k = \sum_b N_b \dot{d}_{k,b} + g_k$ and separating the unknown $\dot{\mathbf{d}}$ from the known terms:

$$\sum_b \left(\int_{\Omega} N_a N_b d\Omega \right) \dot{d}_{k,b} + \int_{\Omega} N_a [(v \cdot \nabla) v_k - \nu \nabla^2 v_k] d\Omega = 0. \quad (6)$$

Applying integration by parts to the viscous term ($\int_{\Omega} N_a \nabla^2 v_k d\Omega = - \int_{\Omega} \nabla N_a \cdot \nabla v_k d\Omega + \int_{\partial\Omega} N_a \partial_n v_k d\Gamma$; the boundary integral vanishes on Dirichlet boundaries where the velocity

is prescribed by constraints, and provides the natural zero-stress condition on free-outflow boundaries) and collecting the coefficients, we obtain the semi-discrete system

$$\mathbf{M} \dot{\mathbf{d}} = -\mathbf{r}_{\text{conv}}(\mathbf{d}) - \nu \mathbf{K} \mathbf{d}, \quad (7)$$

with the global operators

$$M_{ij} = \int_{\Omega} N_i N_j d\Omega \quad (\text{mass matrix}), \quad (8)$$

$$K_{ij} = \int_{\Omega} \nabla N_i \cdot \nabla N_j d\Omega \quad (\text{stiffness matrix}), \quad (9)$$

$$r_{\text{conv},i} = \int_{\Omega} N_i [(\mathbf{v} \cdot \nabla) \mathbf{v}] d\Omega \quad (\text{convective residual}). \quad (10)$$

In practice, the global integrals decompose as sums of element contributions, e.g. $M_{ij} = \sum_e \int_{\Omega_e} N_i N_j d\Omega_e$, evaluated on the reference element with the appropriate Gauss quadrature ruleCa. Both \mathbf{M} and \mathbf{K} have a block-diagonal structure $\text{diag}(\mathbf{M}_s, \mathbf{M}_s)$ and $\text{diag}(\mathbf{K}_s, \mathbf{K}_s)$, reflecting the independent interpolation of v_x and v_y . The convective residual is quadratic in \mathbf{d} and must be reassembled at each time step.

The variational structure of the PMPG formulation endows these operators with favorable properties. The mass matrix \mathbf{M} is symmetric positive definite, and the stiffness matrix \mathbf{K} is symmetric positive semi-definite, since $\mathbf{d}^T \mathbf{K} \mathbf{d} = \int_{\Omega} |\nabla \mathbf{v}|^2 d\Omega \geq 0$. It follows that any linear combination $\mathbf{M} + \alpha \mathbf{K}$ with $\alpha \geq 0$ is symmetric positive definite, a property that guarantees well-posedness of the time-stepping system derived below.

Constrained instantaneous problem. Equation (7) is an instantaneous condition: at each time t , the velocity field \mathbf{d} is known, and the velocity rate $\dot{\mathbf{d}}$ is the unknown to be determined. The solution must additionally satisfy the incompressibility constraint and boundary conditions. These constraints are all linear in \mathbf{d} (trivially so for Dirichlet boundary conditions, and as a consequence of the subparametric geometry mapping for the divergence constraint; see Section 2.3.4) and can be collected as

$$\mathbf{C} \mathbf{d} = \mathbf{b}, \quad (11)$$

where \mathbf{C} is the global constraint matrix and \mathbf{b} the prescribed values; the specific construction of \mathbf{C} and \mathbf{b} is detailed in Sections 2.4 and 2.5. Since the current state satisfies $\mathbf{C} \mathbf{d} = \mathbf{b}$, the constraint on the rate of change is $\mathbf{C} \dot{\mathbf{d}} = \mathbf{0}$, i.e., the velocity rate must itself be divergence-free and must not alter the prescribed boundary values.

The procedure is then, in principle: solve (7) for $\dot{\mathbf{d}}$ subject to $\mathbf{C} \dot{\mathbf{d}} = \mathbf{0}$, update $\mathbf{d}^{n+1} = \mathbf{d}^n + \Delta t \dot{\mathbf{d}}$, and repeat.

Time discretization. A key feature of the present formulation is that the forward Euler discretization $\dot{\mathbf{d}} \approx (\mathbf{d}^{n+1} - \mathbf{d}^n)/\Delta t$ transforms the semi-discrete equation (7) into a system for \mathbf{d}^{n+1} directly. This is significant because \mathbf{d}^{n+1} is the quantity to which we apply the constraints: replacing $\mathbf{C} \dot{\mathbf{d}} = \mathbf{0}$ with $\mathbf{C} \mathbf{d}^{n+1} = \mathbf{b}$ is exact, and the constrained system can be solved in a single monolithic step (Section 2.6).

Substituting the forward Euler discretization into (7) yields a fully explicit time step: $\mathbf{M} \mathbf{d}^{n+1} = \mathbf{M} \mathbf{d}^n - \Delta t \mathbf{r}_{\text{conv}} - \nu \Delta t \mathbf{K} \mathbf{d}^n$. For numerical stability, we replace the explicit viscous term $-\nu \mathbf{K} \mathbf{d}^n$ with the implicit evaluation $-\nu \mathbf{K} \mathbf{d}^{n+1}$, yielding the semi-implicit system

$$(\mathbf{M} + \nu \Delta t \mathbf{K}) \mathbf{d}^{n+1} = \mathbf{M} \mathbf{d}^n - \Delta t \mathbf{r}_{\text{conv}}(\mathbf{d}^n). \quad (12)$$

This removes the diffusive stability constraint $\Delta t \sim h^2/\nu$, leaving only the convective CFL condition $\Delta t \sim h/|\mathbf{v}|$. The modification does not change the steady-state solution (where $\mathbf{d}^{n+1} = \mathbf{d}^n$) and is essential for practical computations at moderate Reynolds numbers.

Remark 2.1. The semi-implicit system (12) has a structural property that distinguishes it from standard Galerkin discretizations. The system matrix $\mathbf{A} = \mathbf{M} + \nu \Delta t \mathbf{K}$ is symmetric positive definite for any positive viscosity and time step, regardless of the Reynolds number: the mass matrix \mathbf{M} is SPD, the stiffness matrix \mathbf{K} is positive semi-definite, and convection appears only in the explicit right-hand side $\mathbf{r}_{\text{conv}}(\mathbf{d}^n)$. Each time step is therefore a constrained minimization of a convex quadratic functional, and the solution is uniquely defined. In Galerkin finite element methods, by contrast, the convection operator contributes an asymmetric term to the system matrix that can violate discrete coercivity when the element Péclet number $\text{Pe}_h = |\mathbf{v}|h/(2\nu) \gg 1$, producing spurious oscillations [10]. The PMPG formulation avoids this mechanism entirely: the CFL condition restricts the time step for temporal accuracy, not for preventing spatial oscillations. Numerical evidence for this property at $Re = 1000$ on coarse meshes with Pe_h up to 42 is presented in Section 4.1.3.

The development above is independent of the specific element type or problem dimension. Next we will detail the specifics of our implementation: the Q9 biquadratic element used for velocity interpolation in 2D problems (Section 2.3), the pointwise divergence-free constraint construction (Section 2.4), boundary conditions (Section 2.5), and the monolithic saddle-point solver that integrates all components (Section 2.6).

2.3 Q9 finite element discretization

The velocity and velocity rate fields are discretized using 9-node biquadratic (Q9) Lagrangian finite elements. Each element carries 9 nodes, and the field is interpolated using the full set of biquadratic shape functions. The coordinate mapping from the reference to the physical element uses a *subparametric* approach detailed in Section 2.3.4.

2.3.1 Reference element

The Q9 element is defined on the reference square $[-1, 1]^2$ with 9 nodes: 4 corners, 4 midside nodes, and 1 center node (Figure 1, left). The reference coordinates (ξ_a, η_a) for each node a are also shown in the figure.

2.3.2 Field interpolation

Any 2D vector field defined at the 9 element nodes is interpolated using the full set of Q9 biquadratic shape functions. In the present formulation, the two fields of interest are the

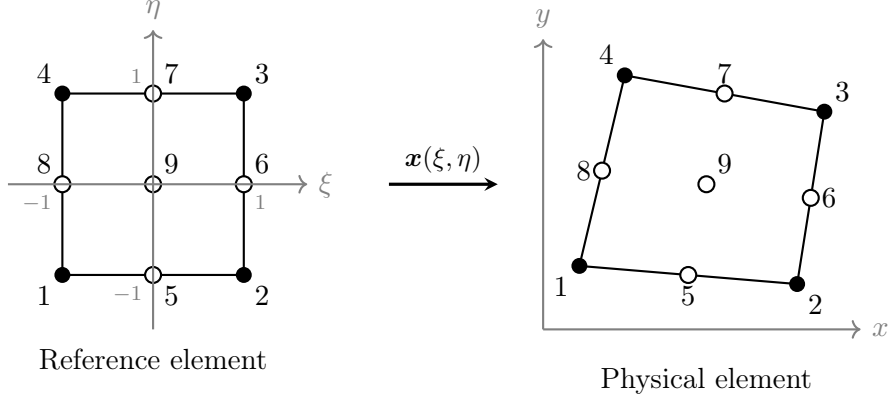


Figure 1: Q9 reference element (left) and a representative physical element (right) under the subparametric mapping $\mathbf{x}(\xi, \eta)$. Filled circles (\bullet) denote the 4 corner nodes that define the bilinear geometry mapping; open circles (\circ) denote the 5 midside and center nodes used only for the biquadratic field interpolation. In the physical element, the midside nodes lie at the midpoints of the (straight) edges, and the center node lies at the intersection of the bimedians, as determined by the bilinear map.

velocity \mathbf{v} and its time derivative $\partial_t \mathbf{v}$; both are interpolated with the same shape functions but with different nodal coefficients.

The shape functions are constructed as tensor products of 1D quadratic Lagrange polynomials on $\{-1, 0, 1\}$:

$$l_0(t) = \frac{t(t-1)}{2}, \quad l_1(t) = 1 - t^2, \quad l_2(t) = \frac{t(t+1)}{2}. \quad (13)$$

The 2D shape functions are $N_a(\xi, \eta) = l_{i_a}(\xi) l_{j_a}(\eta)$ for $a = 1, \dots, 9$, where (i_a, j_a) are the 1D basis indices associated with node a . A generic vector field $\mathbf{f} = (f_x, f_y)$ is then represented by its nodal coefficient vector

$$\mathbf{c} = (c_1, \dots, c_9, c_{10}, \dots, c_{18})^T \in \mathbb{R}^{18}, \quad (14)$$

so that

$$f_x(\xi, \eta) = \sum_{a=1}^9 N_a c_a, \quad f_y(\xi, \eta) = \sum_{a=1}^9 N_a c_{9+a}. \quad (15)$$

For the velocity field, $\mathbf{c} = \mathbf{d}$ with $\mathbf{d} = (v_x^1, \dots, v_x^9, v_y^1, \dots, v_y^9)^T$; for the time derivative, $\mathbf{c} = \dot{\mathbf{d}}$ with $\dot{\mathbf{d}} = (\dot{v}_x^1, \dots, \dot{v}_x^9, \dot{v}_y^1, \dots, \dot{v}_y^9)^T$.

2.3.3 Physical gradients

Computing physical derivatives of the interpolated fields requires the Jacobian \mathbf{J} of the coordinate mapping from the reference element to the physical element. For a scalar component f with nodal values (c_1, \dots, c_9) , the physical derivatives are:

$$\frac{\partial f}{\partial x} = \frac{j_{22}f_{,\xi} - j_{21}f_{,\eta}}{\det(\mathbf{J})}, \quad \frac{\partial f}{\partial y} = \frac{-j_{12}f_{,\xi} + j_{11}f_{,\eta}}{\det(\mathbf{J})}, \quad (16)$$

where $f_{,\xi} = \mathbf{B}_\xi \cdot \mathbf{c}$ and $f_{,\eta} = \mathbf{B}_\eta \cdot \mathbf{c}$, with \mathbf{B}_ξ and \mathbf{B}_η the row vectors of parametric shape function derivatives:

$$\mathbf{B}_\xi = \left(\frac{\partial N_1}{\partial \xi} \quad \cdots \quad \frac{\partial N_9}{\partial \xi} \right), \quad \mathbf{B}_\eta = \left(\frac{\partial N_1}{\partial \eta} \quad \cdots \quad \frac{\partial N_9}{\partial \eta} \right). \quad (17)$$

Applying (16) to each component of \mathbf{v} or $\partial_t \mathbf{v}$ yields the corresponding physical gradient tensor. The Jacobian components j_{ij} and $\det(\mathbf{J})$ depend on the specific geometry mapping, which we detail next.

2.3.4 Subparametric geometry mapping

The physical gradient formulas (16) require the Jacobian of a coordinate mapping from the reference element to the physical element. In the standard isoparametric approach, the same biquadratic functions used for velocity interpolation would also map the geometry, producing a Jacobian that is quadratic in (ξ, η) . We instead adopt a *subparametric* mapping that uses bilinear shape functions constructed from the 4 corner nodes only (Figure 1, right):

$$\mathbf{x}(\xi, \eta) = \sum_{a=1}^4 N_a^{\text{lin}}(\xi, \eta) \mathbf{x}_a, \quad N_a^{\text{lin}} = \frac{(1 + \xi_a \xi)(1 + \eta_a \eta)}{4}. \quad (18)$$

The Jacobian matrix of this mapping,

$$\mathbf{J} = \begin{pmatrix} \frac{\partial x}{\partial \xi} & \frac{\partial x}{\partial \eta} \\ \frac{\partial y}{\partial \xi} & \frac{\partial y}{\partial \eta} \end{pmatrix}, \quad (19)$$

depends at most linearly on (ξ, η) . It can be parameterized by 6 scalars:

$$\begin{aligned} j_{11}^0 &= \frac{1}{4}(-x_1 + x_2 + x_3 - x_4), & j_{12}^0 &= \frac{1}{4}(-x_1 - x_2 + x_3 + x_4), \\ j_{21}^0 &= \frac{1}{4}(-y_1 + y_2 + y_3 - y_4), & j_{22}^0 &= \frac{1}{4}(-y_1 - y_2 + y_3 + y_4), \\ h_1 &= \frac{1}{4}(x_1 - x_2 + x_3 - x_4), & h_2 &= \frac{1}{4}(y_1 - y_2 + y_3 - y_4), \end{aligned} \quad (20)$$

so that the Jacobian components at (ξ, η) are:

$$j_{11} = j_{11}^0 + h_1 \eta, \quad j_{12} = j_{12}^0 + h_1 \xi, \quad j_{21} = j_{21}^0 + h_2 \eta, \quad j_{22} = j_{22}^0 + h_2 \xi. \quad (21)$$

The Jacobian determinant is at most linear in (ξ, η) :

$$\det(\mathbf{J}) = J_0 + J_\xi \xi + J_\eta \eta, \quad (22)$$

where $J_0 = j_{11}^0 j_{22}^0 - j_{12}^0 j_{21}^0$, $J_\xi = j_{11}^0 h_2 - j_{21}^0 h_1$, and $J_\eta = h_1 j_{22}^0 - h_2 j_{12}^0$.

Remark 2.2. The subparametric choice is central to the formulation. The physical derivatives (16) involve division by $\det(\mathbf{J})$. In Section 2.4, the divergence constraint $\partial v_x / \partial x + \partial v_y / \partial y = 0$ is formed from these physical derivatives; multiplying through by $\det(\mathbf{J})$ clears the denominator and yields a constraint row that is a linear combination of the products $j_{ij} \partial N_a / \partial \xi_k$, linear in the nodal velocities \mathbf{d} . Because the subparametric Jacobian components j_{ij} are at most bilinear in (ξ, η) , these products remain low-degree polynomials, well-suited to standard Gauss quadrature. An isoparametric formulation with full biquadratic geometry would produce higher-degree Jacobian entries, complicating the constraint structure without benefit for straight-sided or gently curved elements.

2.4 Divergence-free constraint

The incompressibility condition $\nabla \cdot \mathbf{v} = 0$ is the sole element-level constraint in the viscous formulation. At a quadrature point (ξ_k, η_k) , after multiplying through by $\det(\mathbf{J})$ to avoid division by the Jacobian determinant, the constraint becomes:

$$j_{22}v_{x,\xi} - j_{21}v_{x,\eta} - j_{12}v_{y,\xi} + j_{11}v_{y,\eta} = 0. \quad (23)$$

Substituting the parametric derivatives in terms of \mathbf{d} :

$$\mathbf{c}_k^{\text{div}} \cdot \mathbf{d} = 0, \quad \mathbf{c}_k^{\text{div}} = (j_{22}\mathbf{B}_\xi - j_{21}\mathbf{B}_\eta \quad -j_{12}\mathbf{B}_\xi + j_{11}\mathbf{B}_\eta)_k \in \mathbb{R}^{1 \times 18}. \quad (24)$$

This constraint is *linear* in \mathbf{d} because the Jacobian components depend only on the (fixed) corner coordinates, not on the velocity DOFs.

We enforce (24) at 2×2 Gauss quadrature points, yielding 4 constraint rows per element. The 2×2 rule is the minimum order that captures the divergence of the biquadratic velocity field at sufficient points for accuracy, while leaving $18 - 4 = 14$ unconstrained degrees of freedom per element, enough for the velocity to satisfy the momentum equation. A higher-order rule (e.g., 3×3) would impose 9 constraints per element, leaving only 9 free DOFs and over-constraining the global system. The 4 constraint rows are always linearly independent (rank 4) for non-degenerate elements, so none are redundant at the element level.

Remark 2.3. The 2×2 Gauss points have a structural property beyond the DOF-count argument above. Since $(\nabla \cdot \mathbf{v}) \det(\mathbf{J})$ is at most degree (2, 2) in (ξ, η) (the biquadratic shape function derivatives contribute degree 2 and the subparametric Jacobian components are at most linear), its product with any bilinear function $q(\xi, \eta)$ is at most degree (3, 3), which the 2×2 Gauss–Legendre rule integrates exactly. Consequently, if $(\nabla \cdot \mathbf{v}) \det(\mathbf{J}) = 0$ at the four Gauss points, then for *every* bilinear q ,

$$\int_{\Omega_e} (\nabla \cdot \mathbf{v}) q \, d\Omega = 0. \quad (25)$$

Any divergence residual that survives the constraints is therefore L^2 -orthogonal to the bilinear polynomial space $Q_1 = \text{span}\{1, \xi, \eta, \xi\eta\}$ on each element: it has zero mean, zero first moments, and zero bilinear moment. Only high-order polynomial modes remain, and these oscillate within each element and tend to cancel across neighbors rather than accumulate coherently. This “high-pass filtering” of the divergence residual explains why the 2×2 Gauss rule outperforms collocation at points that minimize a per-element leakage measure; see the Kovaszny flow comparison in Section 3.2 and the detailed analysis in Appendix A.

The element constraint rows are assembled into a global constraint matrix \mathbf{C} by scattering through the element DOF map, in the same way that element stiffness matrices are assembled into a global stiffness matrix. Note that the element-level DOF ordering (14) groups all v_x components before all v_y components, whereas the global DOF vector $\mathbf{d} \in \mathbb{R}^{n_{\text{dofs}}}$ uses an interleaved ordering: DOF $2i$ corresponds to v_x at global node i and DOF $2i + 1$ to v_y at global node i . The element DOF map translates between these two orderings during assembly. Each row of \mathbf{C} enforces $\nabla \cdot \mathbf{v} = 0$ at a specific quadrature point in a specific

element. Boundary conditions (Section 2.5) are appended as additional rows of \mathbf{C} , and the complete system is solved via the saddle-point formulation described in Section 2.6.

A key feature of this formulation is that incompressibility is enforced *pointwise* at the quadrature points, not in a weak or averaged sense. The resulting velocity field is exactly divergence-free at every Gauss point in every element. This is a direct consequence of the variational structure: in the PMPG framework, incompressibility enters as an equality constraint on the minimization, and the Lagrange multipliers enforce it exactly. There is no pressure finite element space, no inf-sup condition to satisfy, and no penalty parameter to tune. The number and placement of the constraints are determined entirely by the choice of quadrature rule.

This stands in contrast to mixed velocity–pressure formulations, where incompressibility is enforced weakly: $\int_{\Omega} q \nabla \cdot \mathbf{v} d\Omega = 0$ for all test functions q in a pressure space Q_h . The velocity field in a mixed method is divergence-free only in the L^2 projection onto Q_h , not pointwise. Furthermore, the pressure space must be chosen to satisfy the Babuška–Brezzi inf-sup condition [4, 5]; if it is not, the formulation is unstable and requires pressure stabilization [11]. The present formulation avoids velocity–pressure inf-sup requirements because no pressure space is introduced; instead, robustness depends on the rank/consistency of the pointwise constraint operator and the conditioning of the resulting KKT system.

2.5 Boundary conditions

All boundary conditions in the present formulation are of Dirichlet type: prescribed velocity values at boundary nodes. Each prescribed component adds one row to the global constraint matrix \mathbf{C} and a corresponding entry to the right-hand side \mathbf{b} . Specifically, prescribing $v_{x,i} = \bar{v}_{x,i}$ at node i contributes a row with a single unit entry at DOF $2i$ in \mathbf{C} and the value $\bar{v}_{x,i}$ in \mathbf{b} ; an analogous row is added for any prescribed $v_{y,i}$.

No-slip walls are the special case $\bar{v}_{x,i} = \bar{v}_{y,i} = 0$ (2 constraints per wall node). Inlet profiles are nonzero Dirichlet conditions with values chosen to match the desired inflow (e.g., a parabolic Poiseuille profile). In both cases, the constraint enters the saddle-point system (26) in the same way as the divergence constraints.

At free-outlet boundaries, no constraints are imposed. The velocity at outlet nodes is determined entirely by the element divergence constraints and the PMPG minimization; the solver naturally adjusts the outflow to satisfy incompressibility globally. This is analogous to the “do-nothing” or natural outflow condition in conventional formulations [12].

2.6 Monolithic saddle-point solver

2.6.1 Coupled system

A common approach in computational fluid dynamics is to solve the unconstrained momentum equation (12) first and then project the result onto the constraint manifold (11) in a separate step. This strategy, introduced by Chorin [1] and widely adopted as the projection or fractional-step method [3], is straightforward to implement but introduces a splitting error between the viscous and incompressibility sub-problems that can compromise steady-state accuracy [3]. Exact projection methods without splitting error can also be formulated at

the discrete level by projecting onto the null space of the discrete divergence operator (not including Dirichlet constraints) when an explicit (preferably sparse) divergence-free basis is available; constructing such a basis is straightforward for some staggered discretizations but can be nontrivial in general FE settings [2].

In the present formulation, we instead incorporate the constraints (11) directly into the time step via Lagrange multipliers. As discussed in Section 2.2, the constraint $\mathbf{C}\mathbf{d}^{n+1} = \mathbf{b}$ is equivalent to $\mathbf{C}\dot{\mathbf{d}} = \mathbf{0}$ and is therefore linear in the PMPG optimization variable. Combined with the semi-implicit system (12), this yields a coupled saddle-point system:

$$\underbrace{\begin{pmatrix} \mathbf{A} & \mathbf{C}^T \\ \mathbf{C} & \mathbf{0} \end{pmatrix}}_{\text{saddle-point matrix}} \begin{pmatrix} \mathbf{d}^{n+1} \\ \boldsymbol{\lambda} \end{pmatrix} = \begin{pmatrix} \mathbf{M}\mathbf{d}^n - \Delta t \mathbf{r}_{\text{conv}} \\ \mathbf{b} \end{pmatrix}, \quad (26)$$

where $\mathbf{A} = \mathbf{M} + \nu\Delta t \mathbf{K}$ is the implicit operator, $\mathbf{C} \in \mathbb{R}^{m \times n_{\text{dofs}}}$ is the full constraint matrix (divergence + boundary conditions), \mathbf{b} is the constraint right-hand side (zero for divergence and no-slip, prescribed values for inlet Dirichlet), and $\boldsymbol{\lambda} \in \mathbb{R}^m$ is the vector of Lagrange multipliers.

The first block row of (26) is the constrained momentum equation: the term $\mathbf{C}^T \boldsymbol{\lambda}$ is the discrete analogue of the constraint forces that enforce incompressibility and boundary conditions. The second block row enforces $\mathbf{C}\mathbf{d}^{n+1} = \mathbf{b}$ exactly. This is a standard saddle-point structure [13] that arises naturally from the constrained minimization of the PMPG functional.

2.6.2 Implementation

The saddle-point matrix in (26) is sparse and its sparsity pattern is fixed throughout the simulation. At each time step:

1. The convective residual $\mathbf{r}_{\text{conv}}(\mathbf{d}^n)$ is computed from the current velocity field.
2. The right-hand side $\mathbf{M}\mathbf{d}^n - \Delta t \mathbf{r}_{\text{conv}}$ is assembled.
3. The saddle-point system (26) is solved either by sparse LU factorization (SuperLU) for moderate-size problems, or by preconditioned GMRES for larger systems. The GMRES solver uses a block-triangular preconditioner based on an incomplete LU factorization of \mathbf{A} and an approximate Schur complement $\hat{\mathbf{S}} = \mathbf{C} \text{diag}(\mathbf{M}_L)^{-1} \mathbf{C}^T$, where \mathbf{M}_L is the lumped mass matrix.

Since the matrix \mathbf{A} depends on Δt (through the term $\nu\Delta t \mathbf{K}$), the factorization (or preconditioner) is recomputed only when Δt changes by more than 10%, which typically occurs only a few times during the warm-up phase.

Remark 2.4. The saddle-point system (26) resembles the structure of mixed finite element formulations [13], but differs in two respects. First, the constraint matrix \mathbf{C} encodes both incompressibility and boundary conditions in a single operator; the Lagrange multipliers $\boldsymbol{\lambda}$ are constraint forces from the optimization, not nodal pressure values from a finite element pressure space. Second, each row of \mathbf{C} enforces a pointwise equality (divergence-free at

a specific quadrature point, or a prescribed velocity at a boundary node) rather than the weighted integral $\int_{\Omega} q \nabla \cdot \mathbf{v} d\Omega = 0$ of a mixed formulation. The velocity field therefore satisfies $\nabla \cdot \mathbf{v} = 0$ exactly at all quadrature points, a property confirmed numerically by constraint residuals at machine precision ($\sim 10^{-13}$) in all test cases. An equivalent velocity-only alternative is to parameterize the solution directly in the null space of the discrete divergence operator (with compatibility to the imposed Dirichlet constraints), but constructing a sparse explicit basis is generally the practical bottleneck in non-staggered discretizations [2].

Remark 2.5. The computational complexity per time step is governed by the saddle-point solve. With 2×2 divergence quadrature, each element contributes 4 constraint rows, so the constraint matrix has $m \approx 4n_e + m_{bc}$ rows, where n_e is the number of elements and m_{bc} is the number of boundary DOFs. The total system dimension is $n + m$, where $n = 2n_{\text{nodes}}$ is the number of velocity DOFs. For Q9 meshes on regular grids, $n_e \approx n_{\text{nodes}}/4$ (each interior node is shared by 4 elements), so $m \approx n$, and the saddle-point system is roughly twice the size of the velocity system alone. A sparse direct solver (LU factorization) requires $O((n + m)^{3/2})$ operations in 2D for typical mesh topologies [13]; iterative solvers (e.g., preconditioned GMRES) reduce this to $O(n + m)$ per iteration with an appropriate preconditioner, at the cost of iteration counts that depend on the condition number. Since $\mathbf{A} = \mathbf{M} + \nu \Delta t \mathbf{K}$ is symmetric positive definite, established block preconditioners for saddle-point systems [13] are directly applicable.

2.7 Adaptive CFL time stepping

The time step is determined adaptively by the convective CFL condition:

$$\Delta t = c_{\text{CFL}} \cdot \frac{h_{\min}}{|\mathbf{v}|_{\max}}, \quad (27)$$

where $h_{\min} = \min_e l_{c,e}$ is the global minimum characteristic element length (computed from the shortest edge of the bilinear mapping), $|\mathbf{v}|_{\max}$ is the global maximum velocity magnitude, and $c_{\text{CFL}} = 0.25$ is a safety factor. A ceiling Δt_{\max} prevents unnecessarily large steps during the initial transient when velocities are small.

2.8 Wall force extraction from Lagrange multipliers

The Lagrange multipliers $\boldsymbol{\lambda}$ from the saddle-point system (26) carry physical information about the constraint forces. From the first block row of (26):

$$\mathbf{A} \mathbf{d}^{n+1} + \mathbf{C}^T \boldsymbol{\lambda} = \mathbf{M} \mathbf{d}^n - \Delta t \mathbf{r}_{\text{conv}}, \quad (28)$$

which can be rearranged as:

$$\mathbf{M} \frac{\mathbf{d}^{n+1} - \mathbf{d}^n}{\Delta t} + \mathbf{r}_{\text{conv}} + \nu \mathbf{K} \mathbf{d}^{n+1} = -\frac{\mathbf{C}^T \boldsymbol{\lambda}}{\Delta t}. \quad (29)$$

The left-hand side is the discrete momentum equation; the right-hand side $-\mathbf{C}^T \boldsymbol{\lambda} / \Delta t$ is the total constraint force exerted on the fluid.

Because the constraint matrix \mathbf{C} contains rows of different types (divergence-free, wall boundary conditions, and far-field Dirichlet), the product $\mathbf{C}^T \boldsymbol{\lambda}$ at a given DOF mixes contributions from all constraints that involve that DOF. In particular, divergence rows from elements sharing a wall node contribute to $[\mathbf{C}^T \boldsymbol{\lambda}]_i$ at wall DOFs, but these terms represent volume-averaged pressure-like forces from the incompressibility constraint, not the surface traction at the wall.

The wall surface traction is obtained by isolating the multipliers associated with the wall boundary condition rows. For a no-slip wall, each wall DOF i has a dedicated constraint row $r(i)$ with a single unit entry: $C_{r(i),i} = 1$. The corresponding multiplier $\lambda_{r(i)}$ is the force needed to hold that DOF at zero, precisely the constraint reaction at the wall. By Newton’s third law, the force the fluid exerts on the wall at DOF i is:

$$f_i = \frac{\lambda_{r(i)}}{\Delta t}, \quad i \in \{\text{wall DOFs}\}. \quad (30)$$

For example, if dealing with a lifting body, the total drag and lift on the wall are obtained by summing the x - and y -components over all wall nodes:

$$F_x = \sum_{i \in \text{wall}} f_{2i}, \quad F_y = \sum_{i \in \text{wall}} f_{2i+1}. \quad (31)$$

Importantly, these nodal forces include both pressure and viscous shear contributions: the multiplier $\lambda_{r(i)}$ is the total force needed to maintain the no-slip condition at node i , encompassing the effect of the full stress tensor without requiring separate pressure or viscous stress reconstructions. This provides a natural and accurate mechanism for computing lift and drag without reconstructing the pressure field. Moreover, the availability of nodal forces directly from the Lagrange multipliers makes the formulation particularly attractive for fluid–structure interaction, where these forces serve as the coupling loads applied to the structural solver.

3 Verification

Before applying the formulation to problems of engineering interest, we verify it against two exact solutions of the Navier–Stokes equations. The two tests are chosen to probe complementary aspects of the solver. Poiseuille channel flow has a quadratic velocity profile that lies exactly in the Q9 biquadratic interpolation space; the monolithic solver should therefore recover it to machine precision, providing a stringent test of the constraint enforcement and time-stepping machinery. The Kovasznay flow, by contrast, has an exponential-trigonometric solution that the Q9 space cannot represent exactly; it tests the spatial convergence rate of the discretization on a non-trivial Navier–Stokes solution.

3.1 Poiseuille flow

3.1.1 Problem setup

The first verification test is plane Poiseuille flow in a rectangular channel of height $H = 1$ and length $L = 5$ (Figure 2). The boundary conditions are: no-slip on both walls ($y = 0$

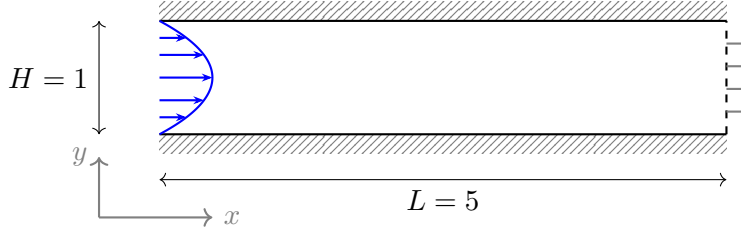


Figure 2: Poiseuille flow: problem setup. Hatched boundaries denote no-slip walls ($\mathbf{v} = \mathbf{0}$), blue arrows indicate the prescribed parabolic inlet profile, and the dashed boundary marks the free outflow.

and $y = H$), parabolic Poiseuille profile at the inlet ($x = 0$),

$$v_x(0, y) = u_{\max} \frac{4y(H - y)}{H^2}, \quad v_y(0, y) = 0, \quad (32)$$

with $u_{\max} = 1.5$ ($U_{\text{mean}} = 1$), and free outflow at $x = L$. The kinematic viscosity is $\nu = 0.1$, giving $Re = H \cdot U_{\text{mean}}/\nu = 10$. The domain is discretized with structured Q9 meshes of $n_x \times n_y$ elements, where $n_x = n_y L/H$ to maintain approximately unit aspect ratio. We report results for $n_y = 4, 8$, and 16 (corresponding to $20 \times 4, 40 \times 8$, and 80×16 element grids).

The simulation is initialized with zero velocity everywhere and advanced in time using the monolithic saddle-point solver (Section 2.6) until a steady state is reached, defined by $\|\partial_t \mathbf{v}\|/\|\mathbf{v}\| < 10^{-12}$.

This problem has a closed-form steady-state solution: $v_x(x, y) = u_{\max} \cdot 4y(H - y)/H^2$, $v_y = 0$, which is a quadratic polynomial in y . Since the Q9 biquadratic interpolation space contains all quadratic polynomials, the exact Poiseuille solution lies in the finite element space. However, membership in the interpolation space is a necessary but not sufficient condition for exact recovery: the time-stepping scheme, constraint enforcement, and saddle-point solver must all preserve the exact solution through the temporal evolution. This makes Poiseuille flow a particularly stringent test of the monolithic formulation.

3.1.2 Results

Figure 3 shows the computed velocity profiles at several x -stations, compared with the exact parabolic profile on the 40×8 mesh. The agreement is visually perfect; the results are indistinguishable on the other meshes.

Quantitatively, the monolithic solver achieves machine-precision accuracy (L^2 error $\sim 10^{-13}$) on all three meshes, confirming that the time-stepping scheme, constraint enforcement, and saddle-point solve introduce no spurious error.

Figure 4 shows the convergence history for the 40×8 mesh. The time-derivative norm $\|\partial_t \mathbf{v}\|$ decreases monotonically and reaches machine precision within approximately 100 time steps, confirming rapid convergence to steady state.

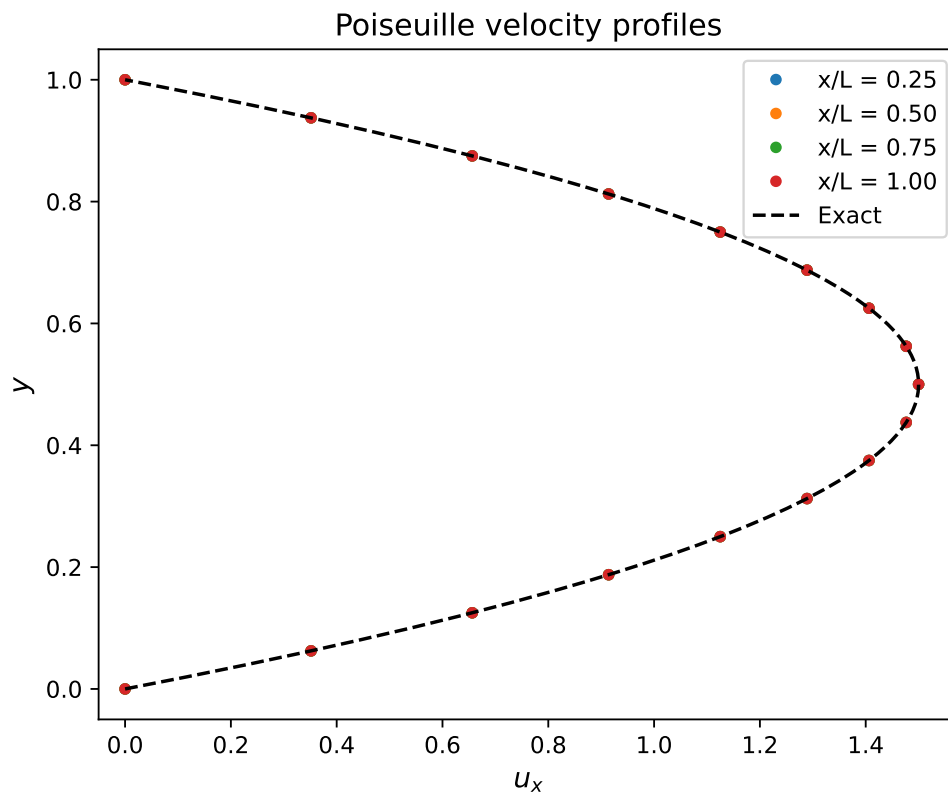


Figure 3: Poiseuille flow: computed velocity profiles (symbols) on the 40×8 mesh compared with the exact parabolic solution (solid line) at multiple x -stations.

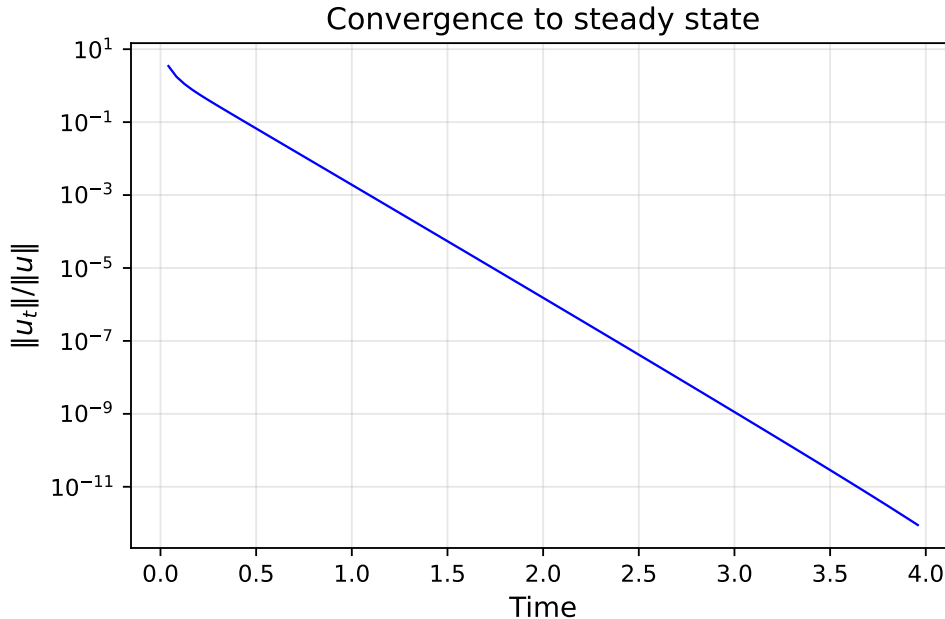


Figure 4: Poiseuille flow: convergence history on the 40×8 mesh. The time-derivative norm $\|\partial_t \mathbf{v}\|$ converges to machine precision, confirming exact steady-state recovery.

3.2 Kovaszny flow

3.2.1 Problem setup

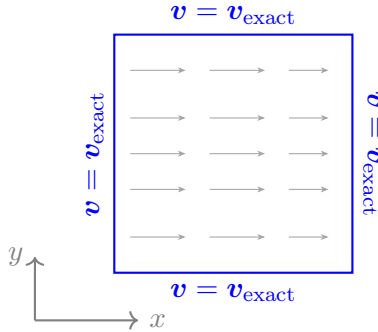
The second verification test uses the exact Kovaszny solution [14], a non-trivial steady-state solution of the incompressible Navier–Stokes equations that describes the flow downstream of a two-dimensional grid. The velocity field is given by:

$$\begin{aligned} v_x &= 1 - e^{\lambda x} \cos(2\pi y), \\ v_y &= \frac{\lambda}{2\pi} e^{\lambda x} \sin(2\pi y), \end{aligned} \quad (33)$$

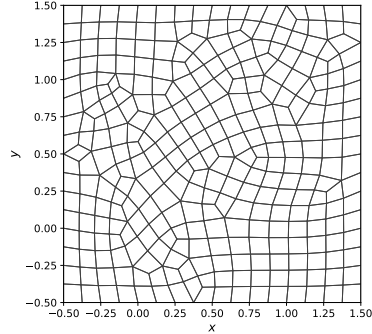
where $\lambda = Re/2 - \sqrt{Re^2/4 + 4\pi^2}$ and $Re = 1/\nu$. The domain is $[-0.5, 1.5]^2$ (Figure 5), and all boundary conditions are Dirichlet with the exact solution prescribed on every edge. There are no solid boundaries; this is a pure spatial accuracy test for the Navier–Stokes operator. We use $Re = 40$ ($\nu = 0.025$).

Unlike Poiseuille flow, the Kovaszny solution contains exponential and trigonometric terms that the Q9 interpolation space cannot represent exactly. The expected convergence rate in the L^2 norm is $O(h^3)$ for biquadratic elements, and the purpose of this test is to verify that the solver attains it.

We perform a spatial convergence study on unstructured Q9 meshes (Figure 5b) with approximate element size $h = 2/n$ for $n = 4, 8, 16$, and 32 . Using unstructured meshes provides a more stringent test of the formulation than a regular grid. Each simulation is initialized with zero velocity and advanced in time using the monolithic solver until the



(a) Problem setup.



(b) Unstructured Q9 mesh ($n = 16,302$ elements).

Figure 5: Kovasznay flow: (a) problem setup: square domain $[-0.5, 1.5]^2$ with the exact Kovasznay solution (33) prescribed as Dirichlet conditions (blue) on all sides; gray arrows indicate the predominantly rightward mean flow; (b) representative unstructured Q9 mesh ($n = 16$).

steady-state criterion $\|\partial_t \mathbf{v}\|/\|\mathbf{v}\| < 10^{-12}$ is met. The L^2 error is then computed via element-wise Gauss quadrature comparing the finite element interpolant to the exact solution (33).

3.2.2 Results

Figure 6 shows the computed velocity streamlines at steady state on the $n = 16$ mesh. The solution exhibits the characteristic Kovasznay pattern: a predominantly rightward flow with exponentially decaying sinusoidal perturbations in the cross-stream direction.

To assess the spatial accuracy, Figure 7 (left) shows the L^2 velocity error as a function of element size h on a log-log scale for the baseline 2×2 Gauss collocation rule. The measured convergence rate ranges from 3.40 on the coarsest pair to 3.18 on the finest, in good agreement with the theoretical $O(h^3)$ expectation for biquadratic elements.

Figure 7 also compares the effect of different collocation-point placements for the divergence constraint (24). Five schemes are tested, all on the same sequence of unstructured meshes: the 2×2 Gauss rule (4 points), the diagonal $(\pm\frac{1}{2}, \pm\frac{1}{2})$ rule (4 points), a cross-axis placement (4 points on the coordinate axes), 2×2 Gauss plus the element center (5 points), and 3×3 Gauss minus the center (8 points). The 2×2 Gauss rule achieves the lowest velocity error and the lowest integrated divergence $\|\nabla \cdot \mathbf{v}\|_{L^2}$ at every refinement level, with clean $O(h^3)$ convergence. The diagonal $(\pm\frac{1}{2}, \pm\frac{1}{2})$ scheme, which minimizes a per-element divergence-leakage measure (Appendix A), produces noticeably higher divergence and degraded velocity accuracy in the assembled system. Over-constrained schemes (5 or 8 points) show no improvement, consistent with the observation that excessive constraints reduce the available DOFs for the momentum equation.

The superiority of the 2×2 Gauss rule in the assembled computation, despite its slightly worse single-element leakage, is explained by the polynomial orthogonality property described in Remark 2.3 and analyzed in detail in Appendix A: the Gauss-point constraints strip the divergence residual of all low-frequency content, so that neighboring-element residuals cancel rather than accumulate.

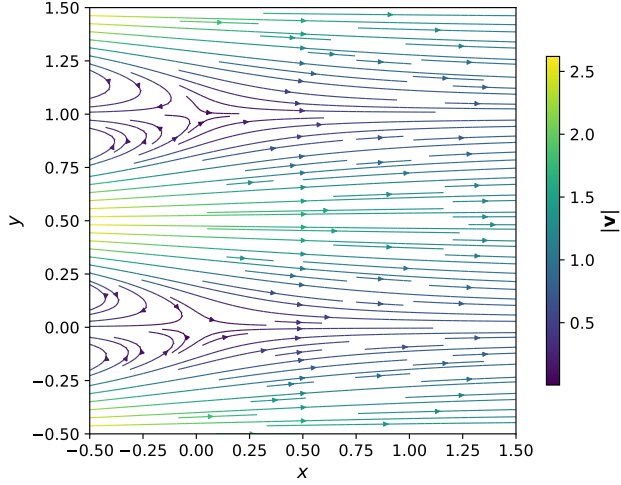


Figure 6: Kovaszny flow: computed velocity streamlines at steady state on the $n = 16$ unstructured mesh.

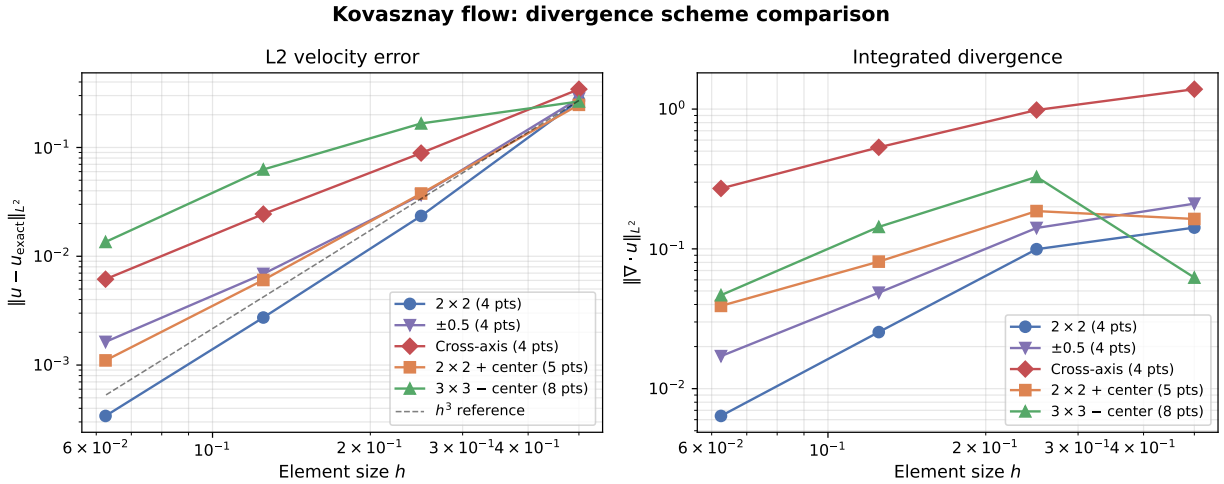


Figure 7: Kovaszny flow: comparison of divergence collocation schemes on unstructured Q9 meshes. **Left:** L^2 velocity error vs. element size h . **Right:** integrated divergence $\|\nabla \cdot \mathbf{u}\|_{L^2}$ vs. h . The 2×2 Gauss rule (blue circles) achieves optimal $O(h^3)$ convergence and the lowest divergence at every refinement level. The polynomial-orthogonality property of the Gauss points (Remark 2.3, Appendix A) prevents low-frequency divergence residuals from accumulating across elements.

4 Demonstrations

Having verified the formulation against exact solutions, we now apply it to benchmark problems of increasing complexity that lack closed-form solutions and must be validated against published experimental or computational data. The lid-driven cavity tests the solver on a confined recirculating flow with velocity singularities at the corners, comparing against the widely used reference data of Ghia et al. [15]. The backward-facing step introduces flow separation and reattachment, exercising the wall force extraction mechanism (Section 2.8) and enabling comparison with the experimental measurements of Armaly et al. [16]. Flow past a circular cylinder validates the drag and lift computation (Section 2.8) against the classical data of Dennis & Chang [17], Tritton [18], and Williamson [19], spanning steady and unsteady regimes.

4.1 Lid-driven cavity

4.1.1 Problem setup

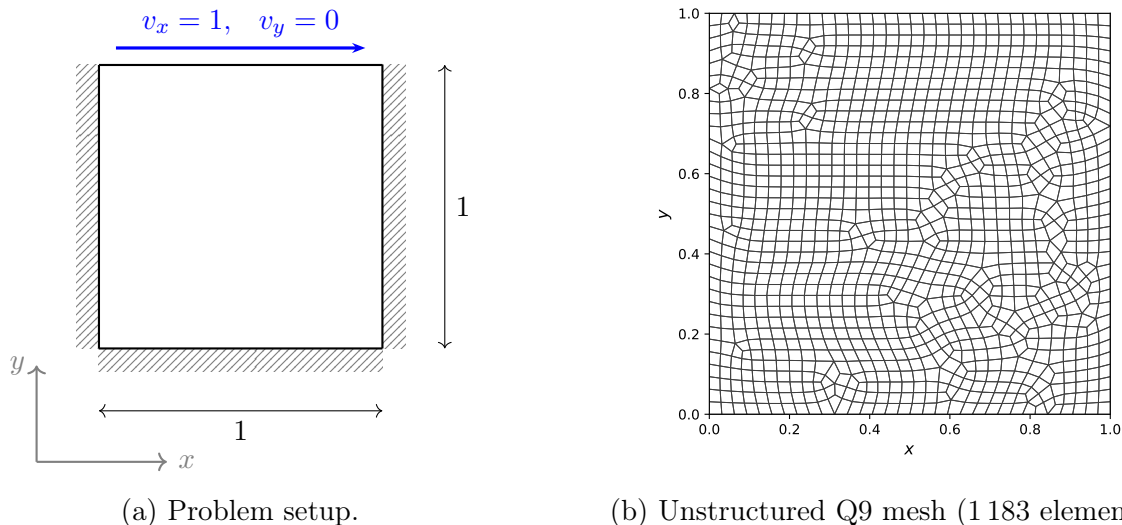


Figure 8: Lid-driven cavity: (a) problem setup: the top wall moves with prescribed velocity (blue arrow) while hatched boundaries denote stationary no-slip walls ($\mathbf{v} = \mathbf{0}$); (b) unstructured Q9 mesh used for both $Re = 100$ and $Re = 400$.

The lid-driven cavity is a standard benchmark for incompressible flow solvers [15, 20]. The domain is $[0, 1]^2$ (Figure 8) with no-slip boundary conditions on all walls. The top wall (lid) moves with unit velocity $v_x = 1$, $v_y = 0$, driving a recirculating flow. The bottom, left, and right walls are stationary ($\mathbf{v} = \mathbf{0}$). At the top corners, where the lid meets the stationary walls, the no-slip condition $\mathbf{v} = \mathbf{0}$ is imposed (wall wins over lid), creating velocity discontinuities that the finite element solution regularizes over nearby elements. The Reynolds number is $Re = U_{\text{lid}}L/\nu$, where $L = 1$ is the cavity side length and $U_{\text{lid}} = 1$ is the lid speed.

For $Re = 100$ ($\nu = 0.01$) and $Re = 400$ ($\nu = 0.0025$), the domain is discretized with an unstructured Q9 mesh of approximately 32×32 elements (Figure 8b; 1 183 elements, 4 861 nodes, 9 722 DOFs). For $Re = 1000$ ($\nu = 0.001$), we use a wall-graded unstructured Q9 mesh with element size $h_{\text{wall}} = 1/32$ at the walls and $h_{\text{center}} = 3/32$ in the interior (446 elements, 1 913 nodes, 3 826 DOFs). Each simulation is initialized with zero velocity and advanced in time using the monolithic solver until the steady-state criterion $\|\partial_t \mathbf{v}\|/\|\mathbf{v}\| < 10^{-10}$ is met. Results are compared against the tabulated reference data of Ghia et al. [15].

4.1.2 Results

Figure 9 presents the computed velocity streamlines (left column, colored by speed $|\mathbf{v}|$) and centerline velocity profiles (right columns, compared with Ghia et al. [15]) at all three Reynolds numbers. At $Re = 100$, a single primary vortex occupies the cavity; at $Re = 400$ the boundary layers thin and secondary corner vortices emerge; at $Re = 1000$ the primary vortex is nearly centered and the corner vortices are more prominent. The centerline profiles show good agreement with the reference data at all three Reynolds numbers, with the velocity gradients near the walls steepening as Re increases.

4.1.3 Stability in the convection-dominated regime

To test the stability of the PMPG formulation at high element Péclet numbers, we solve the cavity at $Re = 1000$ on a sequence of deliberately coarse wall-graded Q9 meshes. Each mesh uses a wall element size $h_{\text{wall}} = 1/n$ and an interior size $h_{\text{center}} = 3/n$, with $n = 12, 16, 24, 32$ elements along each boundary, producing genuinely unstructured meshes ranging from 96 to 446 elements. The element Péclet number at the wall is $Pe_h = Uh_{\text{wall}}/(2\nu) = n/2$, ranging from 6 ($n = 12$) to 16 ($n = 32$); in the interior, where $h_{\text{center}} = 3/n$, Pe_h reaches 42 on the coarsest mesh, well into the regime where standard Galerkin methods exhibit spurious oscillations. Moreover, the laminar boundary layer thickness scales as $\delta \sim L/\sqrt{Re} \approx 0.032$, so that h_{wall}/δ ranges from 2.6 ($n = 12$) to 1.0 ($n = 32$): on the coarsest meshes the boundary layer is not even resolved by a single element.

Despite this severe under-resolution, all four meshes produce smooth, oscillation-free steady-state solutions without any stabilization. Figure 10 overlays the centerline profiles from all four meshes, demonstrating that the solutions converge toward the reference data as the mesh is refined, with no sign of oscillation even on the coarsest grids. This behavior confirms the structural stability property discussed in Remark 2.1: since convection enters only through the explicit right-hand side, the PMPG time-stepping scheme does not suffer from the coercivity loss that triggers Galerkin instabilities at high Péclet numbers.

4.2 Backward-facing step

4.2.1 Problem setup

The backward-facing step is a canonical benchmark for separated flows [16]. The geometry (Figure 11) consists of an L-shaped channel: an inlet section of height $h = H - s$ feeds into an expanded section of height H , with a sharp step of height s at the junction. The expansion

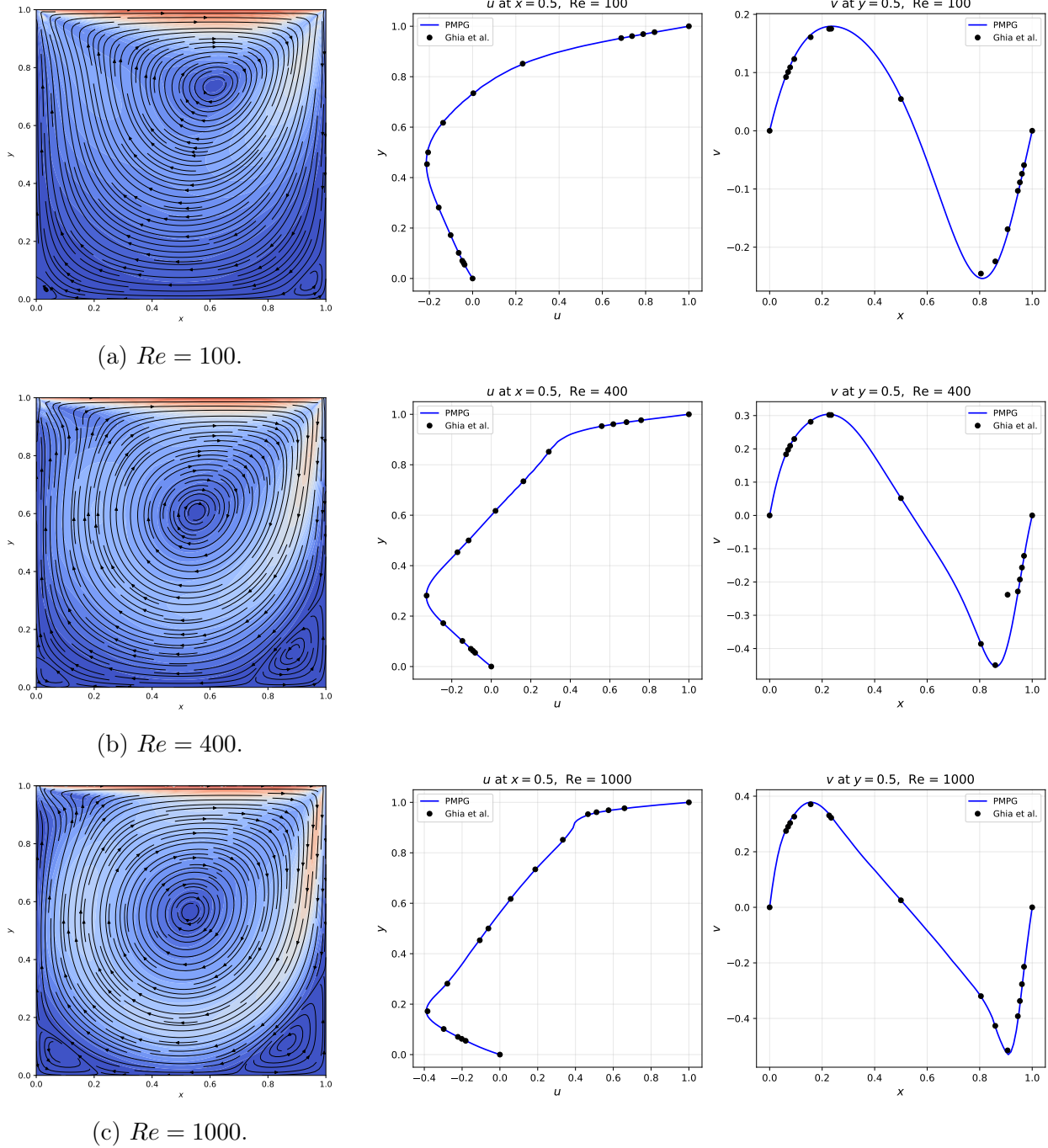


Figure 9: Lid-driven cavity: velocity streamlines colored by speed $|\mathbf{v}|$ (left) and centerline velocity profiles compared with Ghia et al. [15] reference data (symbols, right). As Re increases, the primary vortex migrates toward the center, the boundary layers thin, and secondary corner vortices become more prominent. The PMPG solution agrees well with the reference data at all three Reynolds numbers.

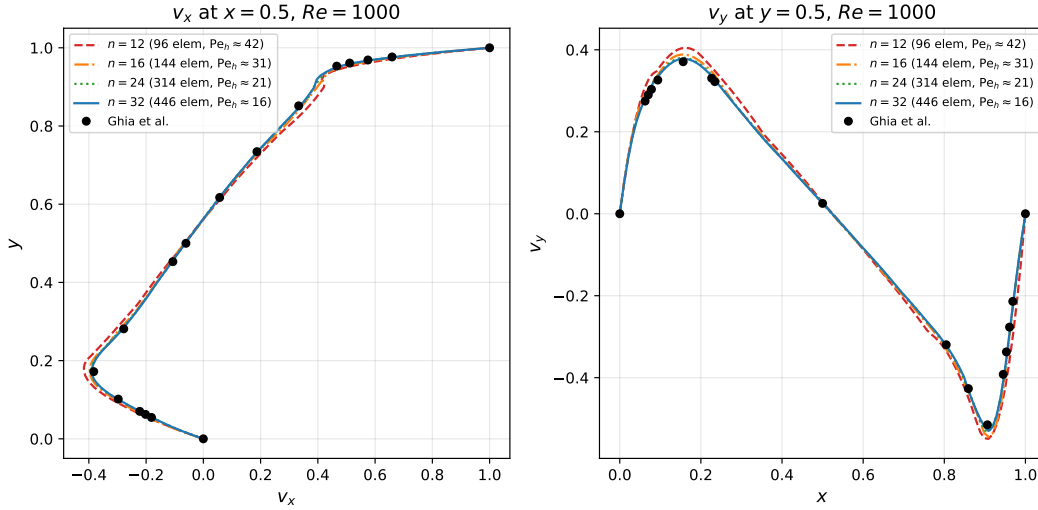
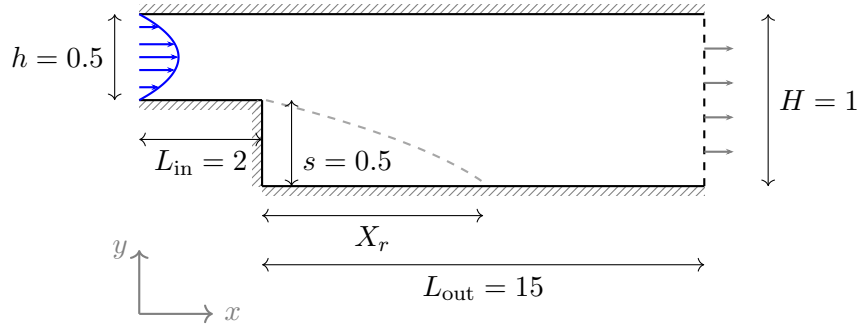
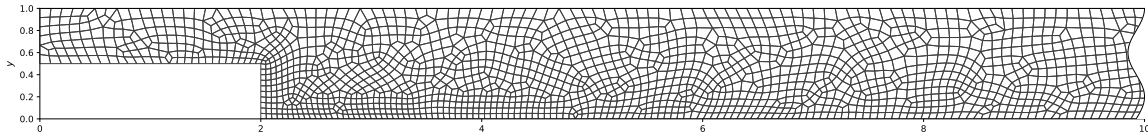


Figure 10: Lid-driven cavity at $Re = 1000$: centerline velocity profiles on coarse wall-graded meshes with $n = 12, 16, 24, 32$ elements per side. Element Péclet numbers range from 16 to 42 in the interior, and the boundary layer is not resolved by a single element on the coarsest meshes. All solutions are smooth and oscillation-free despite the absence of any stabilization, converging toward the Ghia et al. [15] reference data with mesh refinement.



(a) Problem setup.



(b) Unstructured Q9 mesh (2757 elements, $l_c = 0.1$).

Figure 11: Backward-facing step: (a) problem setup: an inlet channel of height $h = 0.5$ feeds into an expanded channel of height $H = 1$ past a step of height $s = 0.5$; blue arrows indicate the parabolic inlet profile, hatched boundaries denote no-slip walls, and the dashed boundary marks the free outflow; the dashed curve indicates the recirculation region with reattachment length X_r ; (b) unstructured Q9 mesh used for $Re = 141$.

ratio is $ER = H/h$. We use $H = 1$, $s = 0.5$ ($ER = 2$, $h = 0.5$), inlet length $L_{\text{in}} = 2$, and outlet length $L_{\text{out}} = 15$ (sufficiently long to avoid outlet effects on the recirculation region).

Boundary conditions are: Poiseuille inlet profile $v_x = \frac{3}{2}U_{\text{mean}} \cdot 4(y-s)(H-y)/h^2$, $v_y = 0$ with $U_{\text{mean}} = 1$; no-slip on all walls (top, bottom, and step face); free outflow at the outlet. The Reynolds number is defined as $Re = U_{\text{mean}} \cdot h/\nu$.

The domain is discretized with unstructured Q9 meshes generated by gmsh (Figure 11b), with the mesh refined near the step corner where the shear layer originates. The characteristic element size is $l_c = 0.15$ for $Re \leq 100$ and $l_c = 0.1$ for $Re = 141$, yielding approximately 1260 and 2760 elements, respectively. Each simulation is initialized with zero velocity and advanced in time using the monolithic solver until the steady-state criterion $\|\partial_t \mathbf{v}\|/\|\mathbf{v}\| < 10^{-10}$ is met.

4.2.2 Results

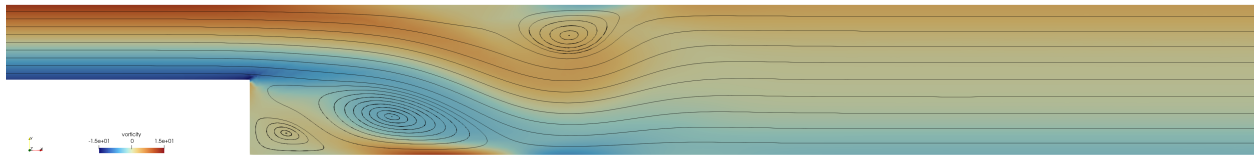
We compute solutions for several Reynolds numbers in the range $Re = 34$ – 141 and compare against the experimental data of Armaly et al. [16] ($ER = 1.94$).

Figure 12 illustrates the transient flow development at $Re = 141$. At step 1000 (panel a), three distinct recirculation zones are visible: two separate bubbles behind the step corner and a third vortex along the upper wall, driven by the separated shear layer. By step 1600 (panel b), the two corner bubbles have merged into a single larger recirculation zone while the upper-wall vortex is convected downstream. Panel (c) shows the final steady state, featuring the characteristic primary recirculation region extending from the step corner. This transient evolution is representative of the rich separated flow dynamics captured by the PMPG formulation.

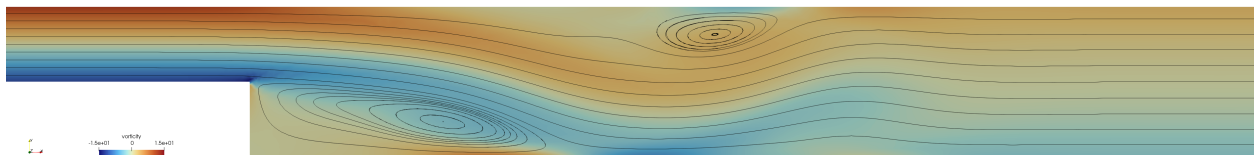
At steady state, flow separates at the step corner and reattaches downstream, forming a recirculation bubble. The primary quantity of interest is the nondimensional reattachment length X_r/s , defined as the distance from the step corner to the reattachment point, normalized by the step height s .

The reattachment point is determined from the wall force extraction mechanism of Section 2.8. When bottom-wall nodes are treated as no-slip constraints, the Lagrange multipliers from the saddle-point system (26) provide the nodal reaction forces via (30). The tangential (streamwise) component at each wall node is directly related to the local wall shear stress: it is negative in the recirculation region, where the flow is reversed, and positive downstream of the reattachment point. The sign change locates the reattachment.

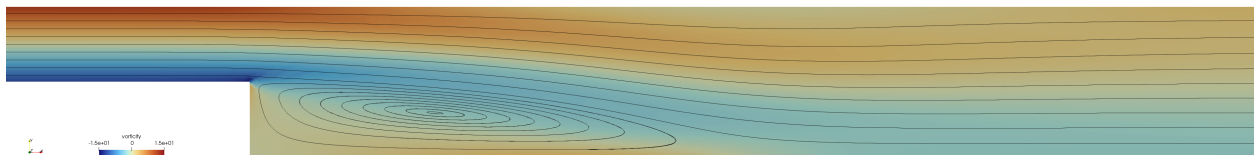
Figure 13 illustrates this for $Re = 100$ by converting the nodal tangential forces to a skin friction coefficient $C_f = 2f_x/(\Delta x_i U_{\text{mean}}^2)$, where f_x is the tangential nodal force from (30) and Δx_i is the tributary length (the Gauss–Lobatto integration weight along the element edge). For validation, the figure also shows the classical stress-based estimate $C_f = 2\nu(\partial v_x/\partial y)|_{y=0}/U_{\text{mean}}^2$, computed from the velocity gradients using the Q9 shape function derivatives. The two distributions are virtually indistinguishable. The relative L^2 error over the full wall, defined as $\|C_f^\lambda - C_f^{\text{stress}}\|_2 / \|C_f^{\text{stress}}\|_2$, is 0.5%; restricting to the region $x/s > 1$ (away from the step-corner singularity where both methods give near-zero values), the median pointwise relative error is 0.03%. This confirms that the Lagrange multiplier wall forces faithfully reproduce the viscous shear stress without requiring explicit velocity gradient evaluation, and that the nodal forces can be used to detect flow features such as



(a) Transient streamlines (step 1000): two corner bubbles and an upper-wall vortex.



(b) Transient streamlines (step 1600): corner bubbles merged, upper vortex convecting downstream.



(c) Steady-state streamlines.

Figure 12: Backward-facing step at $Re = 141$: transient evolution of the velocity streamlines showing the development and merging of recirculation zones. Only the region $x \leq 10$ is shown; the full domain extends to $x = 17$ ($L_{\text{out}} = 15$).

separation and reattachment.

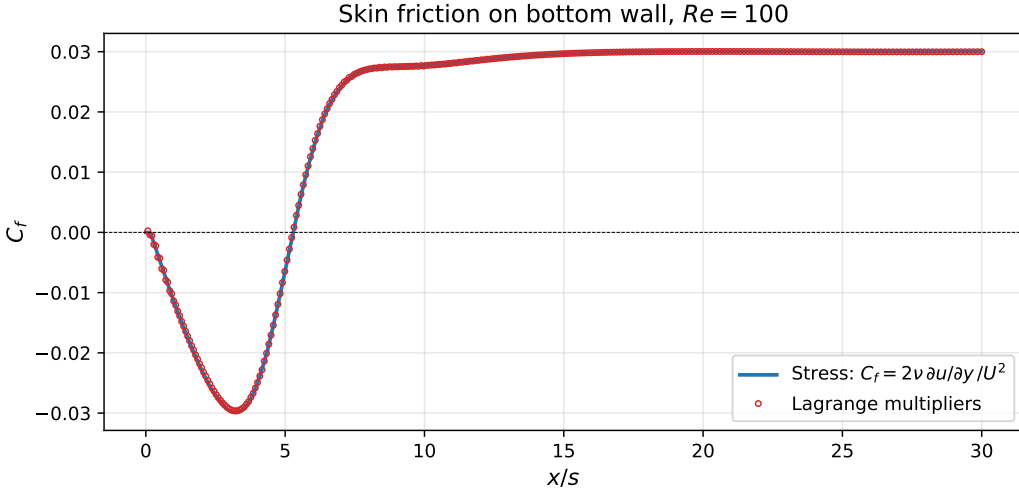


Figure 13: Backward-facing step at $Re = 100$: skin friction coefficient along the bottom wall. Solid line: classical stress-based computation from velocity gradients; circles: Lagrange multiplier nodal forces converted to C_f . The zero crossing indicates the reattachment point.

Figure 14 collects the nondimensional reattachment lengths for all Reynolds numbers considered. The PMPG results follow the expected linear trend $X_r/s \propto Re$ in good agreement with both experimental datasets despite the slight differences in expansion ratio. At lower Reynolds numbers ($Re \leq 100$), the error relative to the nearest experimental value is below 7%, with the best agreement at $Re \approx 48$ (1.1% error). At $Re = 141$ the error is 4.6%, consistent with the increased complexity of the flow at higher Reynolds numbers.

4.3 Flow past a circular cylinder

4.3.1 Problem setup

Flow past a circular cylinder is a classical benchmark that spans qualitatively different flow regimes as the Reynolds number increases: steady symmetric flow ($Re \lesssim 5$), steady recirculation with twin vortices ($5 \lesssim Re \lesssim 47$), and periodic vortex shedding ($Re \gtrsim 47$) [19]. We consider three Reynolds numbers that sample these regimes: $Re = 20$ and $Re = 40$ (steady, twin vortices), and $Re = 100$ (unsteady, vortex shedding).

The computational domain (Figure 15) is $[-15D, 25D] \times [-15D, 15D]$, with the cylinder of diameter $D = 1$ centered at the origin. Boundary conditions are: uniform inflow $\mathbf{v} = (U_\infty, 0)$ with $U_\infty = 1$ on the left boundary; freestream velocity $\mathbf{v} = (U_\infty, 0)$ on the top and bottom boundaries; no-slip ($\mathbf{v} = \mathbf{0}$) on the cylinder surface; and free outflow on the right boundary. The Reynolds number is defined as $Re = U_\infty D / \nu$.

The domain is discretized with unstructured Q9 meshes generated by gmsh, with far-field characteristic element size $l_c = 0.3$, refined to $l_c/4 \approx 0.075$ at the cylinder surface. This yields approximately 26 000 elements and 106 000 nodes (212 000 velocity DOFs). Each simulation

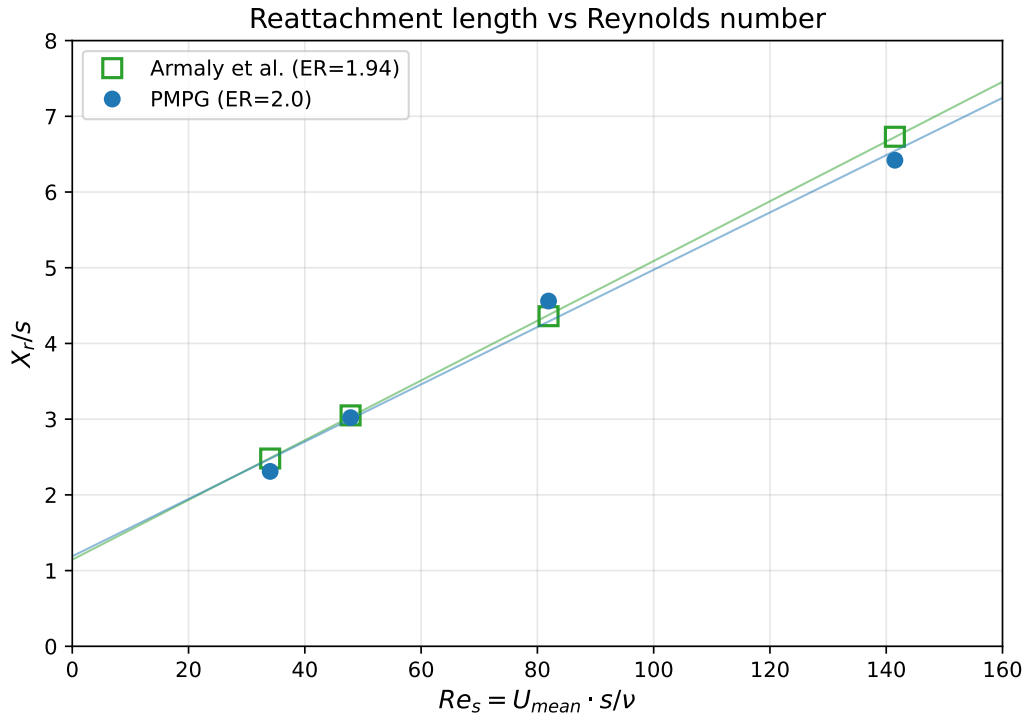


Figure 14: Backward-facing step: nondimensional reattachment length X_r/s as a function of Reynolds number. PMPG results (circles with least-squares fit) compared with experimental data of Armaly et al. [16].

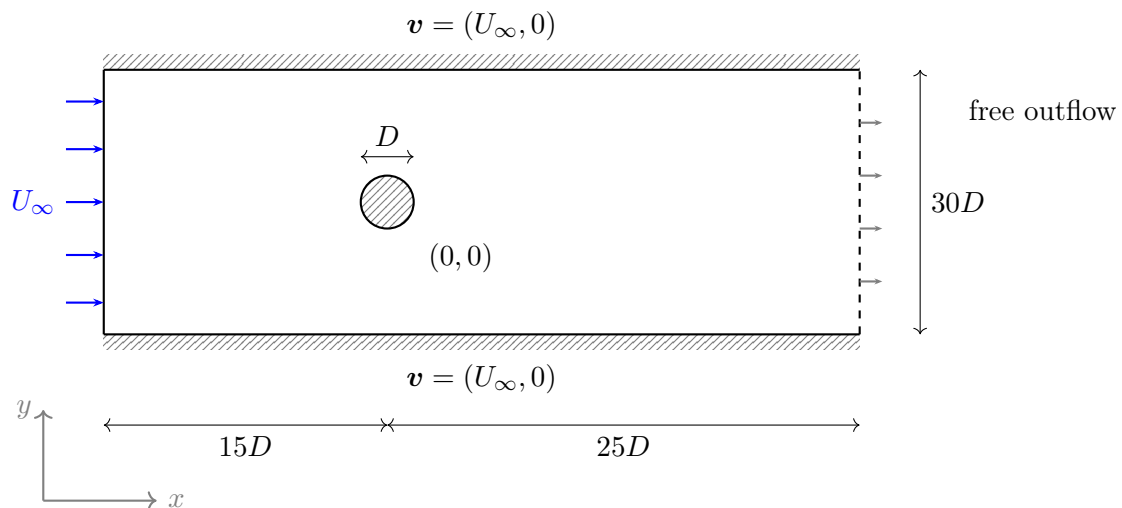


Figure 15: Flow past a circular cylinder: computational domain (not to scale). Uniform inflow $U_\infty = 1$ on the left, freestream velocity $\mathbf{v} = (U_\infty, 0)$ on the top and bottom, no-slip on the cylinder surface, and free outflow on the right. The cylinder of diameter $D = 1$ is centered at the origin.

is initialized with uniform flow $\mathbf{v} = (U_\infty, 0)$ everywhere (with $\mathbf{v} = \mathbf{0}$ on the cylinder) and advanced in time using the monolithic solver with adaptive CFL time stepping ($c_{\text{CFL}} = 0.25$).

Drag and lift coefficients are defined as:

$$C_D = \frac{F_x}{\frac{1}{2}\rho U_\infty^2 D}, \quad C_L = \frac{F_y}{\frac{1}{2}\rho U_\infty^2 D}, \quad (34)$$

where F_x and F_y are the total wall forces from (31) and the reference length is the cylinder diameter D (standard 2D convention, per unit span).

4.3.2 Results

At $Re = 20$ and $Re = 40$, the flow reaches a steady state. Table 1 compares the computed drag coefficients with the numerical results of Dennis & Chang [17] and the experimental measurements of Tritton [18]. At $Re = 20$ the present result ($C_D = 2.13$) is within 4% of Dennis & Chang and 2% of Tritton. At $Re = 40$ the computed value ($C_D = 1.57$) is within 3% of Dennis & Chang and 1.3% of Tritton. At $Re = 100$, where the flow is unsteady, the time-averaged drag coefficient ($C_D = 1.36$) is within 3% of Tritton’s experimental measurement.

At $Re = 100$, the flow develops periodic vortex shedding (von Kármán street). Figure 16 compares the steady twin-vortex wake at $Re = 40$ with the fully developed von Kármán vortex street at $Re = 100$.

After an initial transient, the lift coefficient C_L oscillates symmetrically about zero, indicating alternating vortex detachment from the upper and lower surfaces of the cylinder. Figure 17 shows the time history of C_D and C_L . The drag oscillates at twice the shedding frequency (as expected from symmetry), while the lift oscillates at the fundamental frequency.

The Strouhal number characterizing the shedding frequency is:

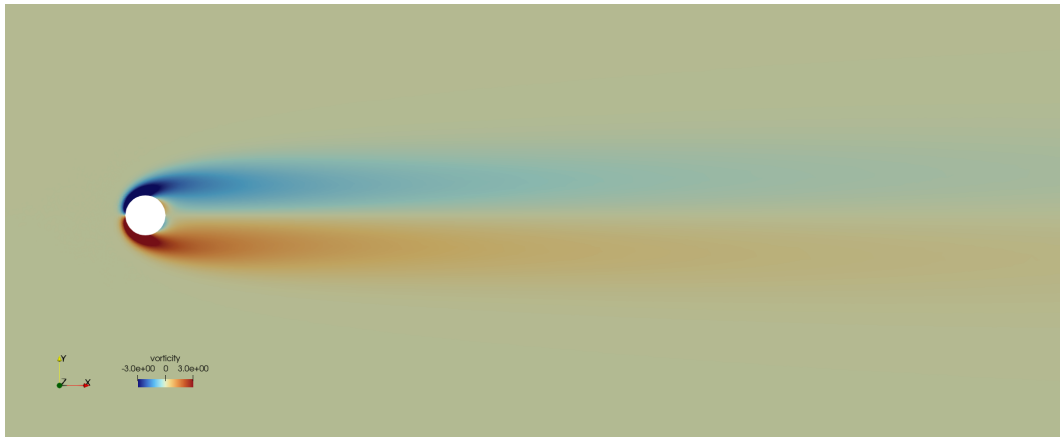
$$St = \frac{fD}{U_\infty}, \quad (35)$$

where f is determined from the zero crossings of the periodic C_L signal, and the reported C_D is the time average over the fully developed oscillatory regime. The computed Strouhal number ($St = 0.168$) agrees to within 2.5% of the experimental correlation of Williamson [19] ($St = 0.164$), as reported in Table 1.

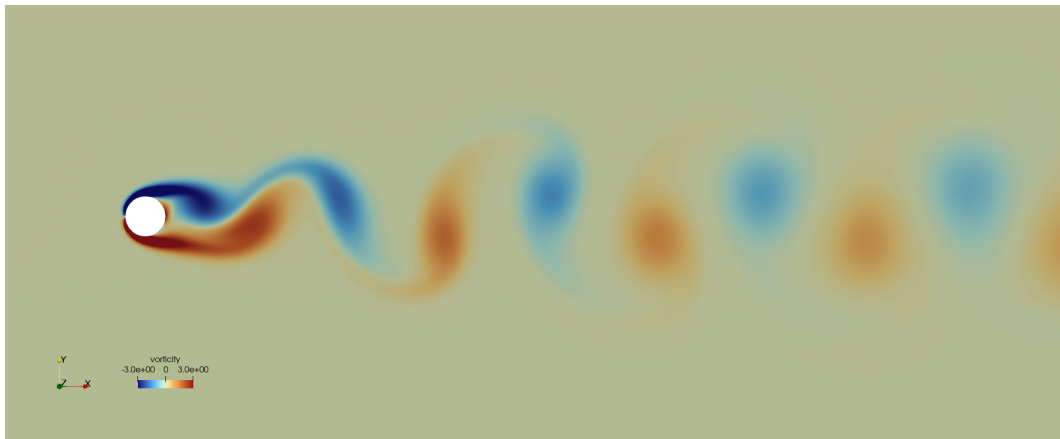
Table 1: Flow past a circular cylinder: drag coefficient C_D and Strouhal number St compared with published data. Dashes indicate quantities not applicable to the flow regime.

Re	C_D			St	
	PMPG	Dennis & Chang	Tritton	PMPG	Williamson
20	2.13	2.045	2.09	—	—
40	1.57	1.522	1.59	—	—
100	1.36	—	1.32	0.168	0.164

The cylinder benchmark demonstrates the wall force extraction mechanism (Section 2.8) on a curved geometry with quantitative validation. The drag coefficients computed from the



(a) $Re = 40$: steady-state symmetric twin-vortex wake.



(b) $Re = 100$: instantaneous von Kármán vortex street.

Figure 16: Flow past a circular cylinder: vorticity contours showing the transition from the steady regime to periodic vortex shedding.

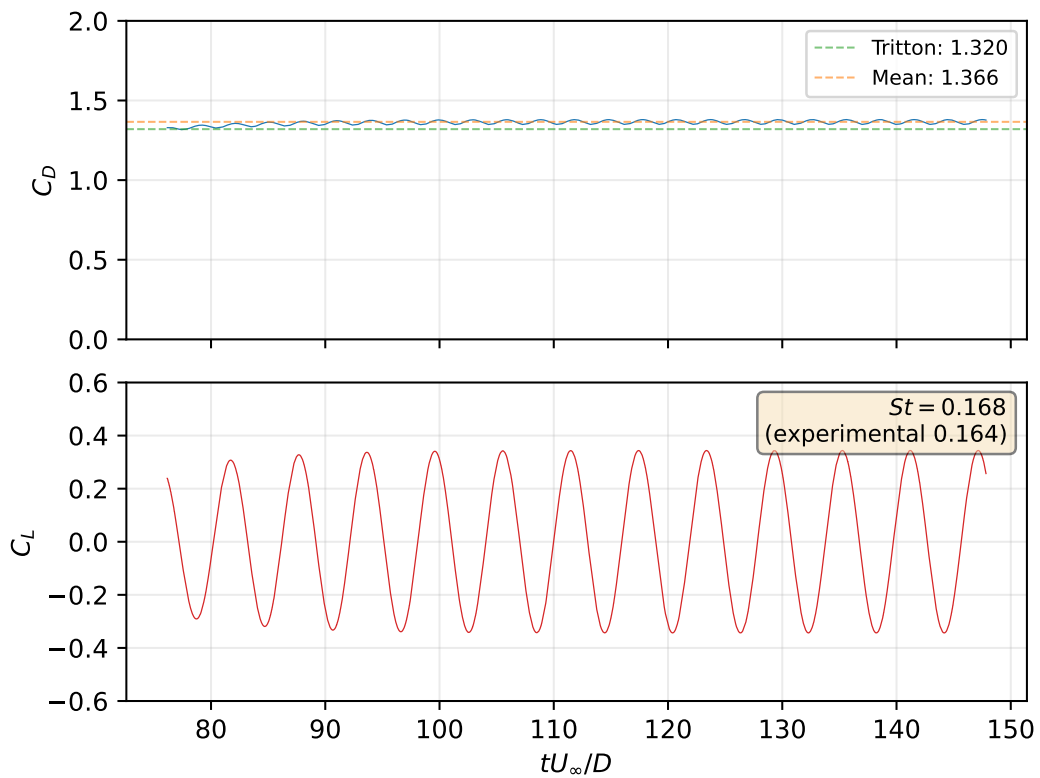


Figure 17: Flow past a circular cylinder at $Re = 100$: time history of (a) drag coefficient C_D and (b) lift coefficient C_L . The periodic oscillations correspond to vortex shedding.

Lagrange multipliers agree with published values without requiring pressure reconstruction or stress integration, confirming that the constraint reactions provide a reliable mechanism for computing aerodynamic forces.

5 Error estimation and adaptive refinement

A distinctive feature of the PMPG formulation is that the objective function itself provides a natural measure of solution quality. The PMPG functional (3) evaluates the squared L^2 norm of the momentum residual, $\mathcal{J}_h = \frac{1}{2} \int_{\Omega} |\mathbf{R}_h|^2 d\Omega$, where $\mathbf{R}_h = (\mathbf{v}_h \cdot \nabla) \mathbf{v}_h - \nu \nabla^2 \mathbf{v}_h$ is the residual (4) evaluated on the discrete velocity field. The exact Navier–Stokes velocity $\mathbf{v}_{\text{exact}}$ has its own residual $\mathbf{R}_{\text{exact}} = (\mathbf{v}_{\text{exact}} \cdot \nabla) \mathbf{v}_{\text{exact}} - \nu \nabla^2 \mathbf{v}_{\text{exact}}$ and the corresponding functional value

$$\mathcal{J}_{\text{exact}} = \frac{1}{2} \int_{\Omega} |\mathbf{R}_{\text{exact}}|^2 d\Omega. \quad (36)$$

The element-wise functional density \mathcal{J}_e/A_e , where A_e is the element area, therefore measures the local momentum imbalance and serves as a built-in error indicator: regions where the residual is large relative to its neighbors signal under-resolution. Unlike residual-based *a posteriori* estimators for Galerkin methods [21, 22], which require reliability and efficiency constants that depend on the local mesh geometry and the PDE coefficients, the PMPG indicator emerges directly from the variational principle (it is the quantity being minimized) and requires no additional computation beyond what the solver already performs.

5.1 Element-wise error indicator

To assess the indicator quantitatively, we return to the Kovaszny test problem (Section 3.2), for which the exact solution is available. Writing $\mathbf{R}_h = \mathbf{R}_{\text{exact}} + \delta \mathbf{R}$, where $\delta \mathbf{R} = \mathbf{R}_h - \mathbf{R}_{\text{exact}}$ is the residual error, the gap between the discrete and exact functionals decomposes as

$$\mathcal{J}_h - \mathcal{J}_{\text{exact}} = \underbrace{\int_{\Omega} \mathbf{R}_{\text{exact}} \cdot \delta \mathbf{R} d\Omega}_{\text{cross term}} + \underbrace{\frac{1}{2} \int_{\Omega} |\delta \mathbf{R}|^2 d\Omega}_{\text{quadratic term} \geq 0}. \quad (37)$$

The quadratic term is non-negative by construction; the cross term can have either sign. For a discrete solution that satisfies the boundary conditions and the divergence constraint exactly, the functional is an upper bound on $\mathcal{J}_{\text{exact}}$. When these constraints are only approximately satisfied, the gap can become negative, signaling that the constraints themselves are under-resolved. This non-monotone behavior is itself a useful diagnostic.

Figure 18 shows the convergence of $\mathcal{J}_h - \mathcal{J}_{\text{exact}}$ and the velocity L^2 error on the Kovaszny problem for mesh sizes $n = 4, 6, 8, 12, 16, 24, 32$. The gap changes sign between $n = 4$ (negative, due to constraint violation on the coarsest mesh) and $n = 6$ (positive), and thereafter converges at a rate $\sim h^2$. The gap decomposition (37) confirms that the cross term drives the sign change on coarse meshes, while the quadratic term, which is always non-negative, dominates on finer meshes.

At the element level, the quadratic component of the gap $\frac{1}{2} \int_{\Omega_e} |\delta \mathbf{R}|^2 d\Omega$ correlates near-perfectly with the true element-wise velocity error. Figure 19 compares, on the $n = 16$ mesh,

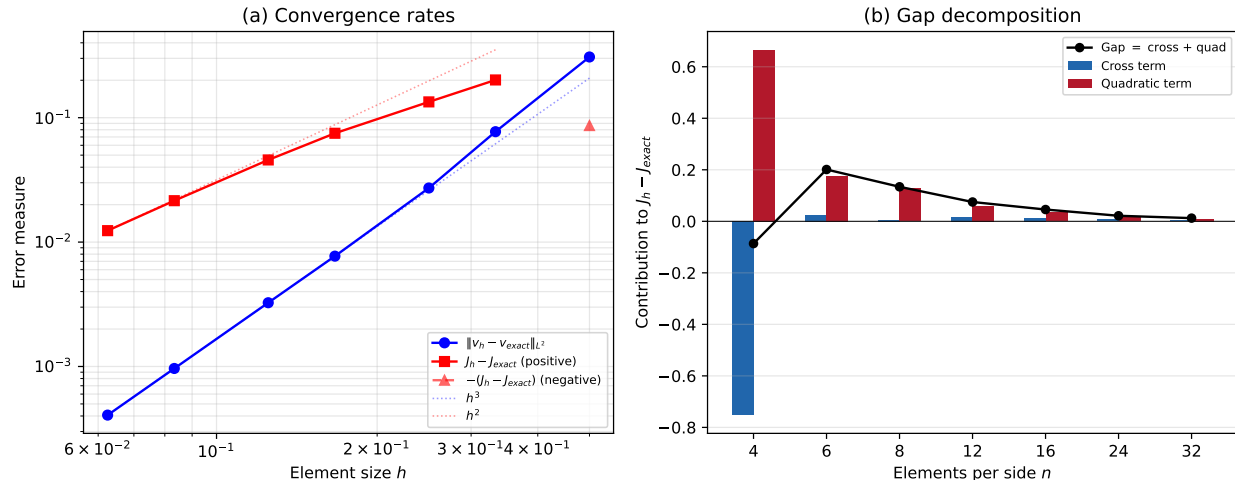


Figure 18: Kovasznay flow: convergence of the PMPG functional. **(a)** Velocity L^2 error and functional gap $\mathcal{J}_h - \mathcal{J}_{\text{exact}}$ versus element size h . The gap changes sign between $n = 4$ and $n = 6$; filled squares denote positive gap, open triangles denote negative gap (plotted as absolute value). Reference slopes h^3 and h^2 are shown. **(b)** Decomposition of the gap into cross and quadratic terms (37). The negative gap on the coarsest mesh is due to the cross term; the quadratic term is always non-negative.

the full element-wise indicator $\eta_e = \mathcal{J}_e - \mathcal{J}_e^{\text{exact}}$ with the element-wise L^2 velocity error, and shows separately the correlation of the quadratic term alone. While the full indicator η_e shows moderate rank correlation (Spearman $\rho = 0.69$) because of sign-indefinite cross terms, the quadratic term achieves $\rho = 0.996$: it is an almost perfect ranker of elements by error magnitude.

Remark 5.1. The Kovasznay test is an unusual case: all boundary conditions involve transcendental functions that the Q9 space cannot represent exactly, leading to constraint violation on coarse meshes and a negative gap at $n = 4$. In typical applications (channel flows, cavity flows, cylinder flows), the boundary conditions are polynomial or zero (no-slip walls), and the Q9 space represents them exactly. In such cases the functional is a true upper bound on $\mathcal{J}_{\text{exact}}$, and monotone decrease with mesh refinement is expected.

5.2 Spatial distribution on the backward-facing step

When no exact solution is available, the functional density \mathcal{J}_e/A_e can still be used as a spatial diagnostic: elements with high density relative to the mesh average are candidates for refinement. Figure 20 shows the element-wise functional density on the backward-facing step ($\text{Re} = 100$, Section 4.2) computed on an unstructured Q9 mesh with characteristic element size $l_c = 0.10$.

The density naturally concentrates at the step corner, a geometric singularity where the velocity gradients are strongest, and along the free shear layer emanating from the step edge. In the fully developed downstream region, the density drops by four orders of magnitude. The indicator therefore identifies, without any additional computation, precisely the flow

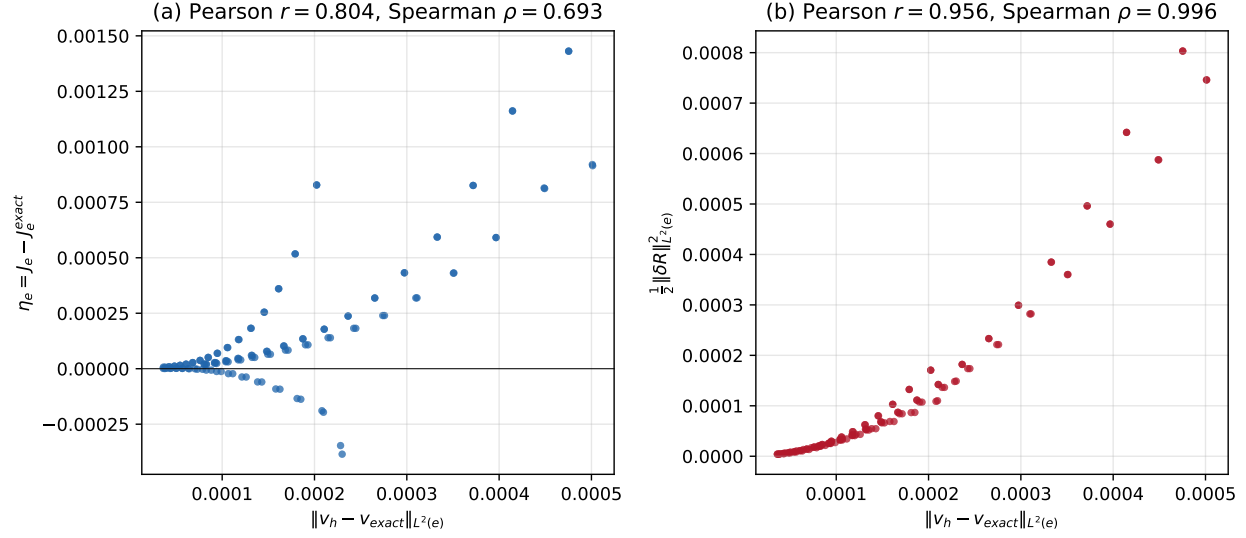


Figure 19: Kovaszny flow ($n = 16$): element-wise error indicator versus true velocity L^2 error. **Left:** Full indicator $\eta_e = \mathcal{J}_e - \mathcal{J}_e^{\text{exact}}$ (Spearman $\rho = 0.69$). **Right:** Quadratic term $\frac{1}{2} \int_{\Omega_e} |\delta \mathbf{R}|^2 d\Omega$ (Spearman $\rho = 0.996$). The quadratic term provides near-perfect element-error ranking.

features that require resolution: the separation point, the shear layer, and the reattachment zone.

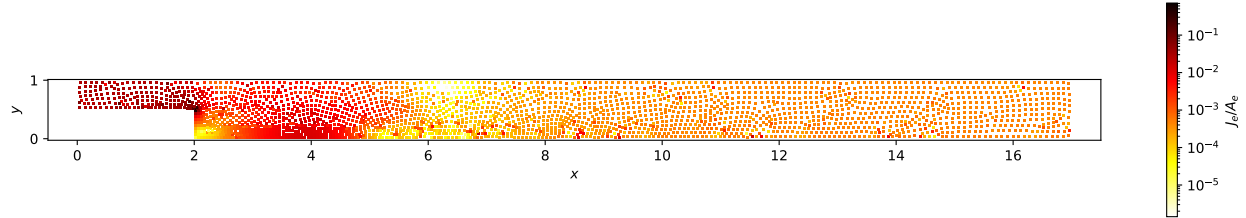


Figure 20: Backward-facing step ($\text{Re} = 100$): element-wise PMPG functional density \mathcal{J}_e/A_e on a logarithmic color scale. The indicator spans four orders of magnitude and concentrates at the step corner, the free shear layer, and the reattachment zone.

5.3 Adaptive mesh refinement

The functional density can drive mesh adaptation through equidistribution: elements with high density are refined, and elements with low density are coarsened, so as to equalize the density across the mesh. Specifically, the target element size is computed as

$$h_e^{\text{new}} = h_e \left(\frac{\bar{\mathcal{J}}}{\mathcal{J}_e/A_e} \right)^\alpha, \quad (38)$$

where $h_e = \sqrt{A_e}$ is the current element size, $\bar{\mathcal{J}}$ is the mean functional density, and $\alpha = 0.25$. The target sizes are clipped to $[h_{\min}, h_{\max}]$, projected from element centers to mesh nodes by

averaging, and passed to Gmsh [23] as a background size field to generate a new Q9 mesh.

Figure 21 compares the mesh topology near the step corner before and after adaptation. The initial uniform mesh ($l_c = 0.15$) contains 886 elements. After a single adaptation cycle, the adapted mesh contains 715 elements (a 19% reduction) while maintaining the same global functional value. The elements concentrate at the step corner and along the shear layer, precisely where the functional density is largest, and coarsen in the developed downstream region where the flow is well resolved.

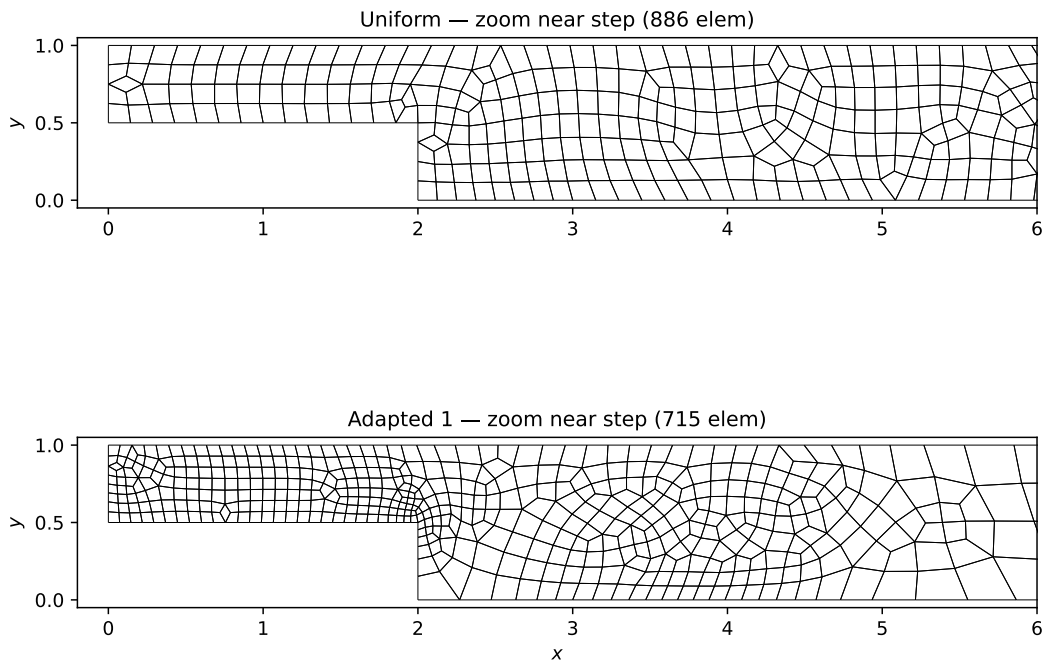


Figure 21: Backward-facing step: mesh topology near the step corner. **Top:** Uniform mesh (886 elements). **Bottom:** After one adaptation cycle (715 elements, -19%). Elements concentrate at the step corner and shear layer, coarsening downstream where the flow is well resolved.

The purpose of this demonstration is not to develop a full adaptive mesh refinement algorithm (issues such as convergence criteria, oscillation control, and optimal refinement strategies are beyond the present scope) but rather to illustrate that the PMPG functional provides a natural, zero-cost error indicator that can drive standard mesh adaptation tools without any additional machinery.

6 Viscosity estimation from velocity field data

Estimating fluid properties from velocity field measurements is an active area of research. Physics-informed neural networks (PINNs) [24, 25] co-learn velocity, pressure, and Navier–Stokes parameters by minimizing PDE residuals through iterative training. Bayesian inverse Navier–Stokes methods [26] reconstruct the full flow field and learn rheological parameters via adjoint-based optimization with uncertainty quantification. These approaches are powerful

and general, but they involve iterative optimization loops and operate on the Navier–Stokes equations in a form that includes pressure as an additional unknown.

In experimental solid mechanics, the Virtual Fields Method (VFM) [27] takes a different approach: it tests the weak form of equilibrium against judiciously chosen virtual displacement fields to extract constitutive parameters directly from full-field strain measurements, without solving any forward problem. No iterative optimization is needed; the unknown parameters appear linearly in the weak form, and the identification reduces to a direct linear solve. Crucially, the weak form involves only first spatial derivatives (strains), not second derivatives, making the method inherently more robust to measurement noise.

The PMPG stationarity condition (7) naturally suggests an analogous approach for fluid viscosity. In the forward solver, this condition determines $\dot{\mathbf{d}}$ for a known ν ; reading it backwards, with the velocity and its time derivative known from experiment, it becomes a constraint on ν . Since the formulation is velocity-only (no pressure field is ever introduced), the measured velocity enters directly into the same finite element operators (\mathbf{M} , \mathbf{K} , \mathbf{r}_{conv}) used in the forward solver. The constraint forces $\mathbf{C}^T \boldsymbol{\lambda}$ are removed by projecting onto the null space of \mathbf{C} , and the viscosity is recovered from a single ratio of inner products. Like the VFM, only first spatial derivatives of the measured velocity are needed (through the stiffness matrix \mathbf{K}), not the Laplacian $\nabla^2 \mathbf{v}$ that appears in the strong-form Navier–Stokes equations. The entire identification is a direct algebraic computation: no forward solve, no adjoint, no iterative optimization.

While the underlying idea (testing a weak momentum balance against divergence-free fields to isolate ν) could in principle be pursued with any consistent Galerkin discretization, the velocity-only PMPG formulation makes the implementation particularly clean: there is no pressure field to reconstruct or eliminate, and the collocation-point divergence constraint (Section 2.4) provides the sparse matrix \mathbf{C}_{div} from which the projector is built via a single sparse factorization.

In this section we develop this idea into a concrete method for identifying the kinematic viscosity from particle image velocimetry (PIV) data. The method is demonstrated on synthetic data (converged numerical solutions used as surrogate PIV measurements, with and without added noise), leaving validation on experimental PIV data for future work.

6.1 Formulation

Consider an experimentalist who has measured the velocity field in a rectangular window at a regular array of points, the typical output of a PIV system. The measured velocities are assigned to a Q9 finite element mesh: each 3×3 block of measurement points defines one biquadratic element. From this mesh, the mass matrix \mathbf{M} , the stiffness matrix \mathbf{K} , the convective residual $\mathbf{r}_{\text{conv}}(\mathbf{d})$, and the divergence constraint matrix \mathbf{C} (Section 2.4) are assembled in the usual way. No boundary conditions are imposed; the only constraint is incompressibility, $\mathbf{C}\mathbf{d} = \mathbf{0}$.

The PMPG stationarity condition (7) extended with the constraint force from incompressibility reads

$$\mathbf{M}\dot{\mathbf{d}} + \mathbf{r}_{\text{conv}}(\mathbf{d}) + \nu \mathbf{K}\mathbf{d} + \mathbf{C}^T \boldsymbol{\lambda} = \mathbf{0}. \quad (39)$$

In the forward solver, ν is known and $\dot{\mathbf{d}}$ is the unknown; here, the velocity and its time

derivative are data and ν is the unknown. Defining

$$\mathbf{a}_h = \mathbf{M}\dot{\mathbf{d}} + \mathbf{r}_{\text{conv}}(\mathbf{d}), \quad \mathbf{b}_h = \mathbf{K}\mathbf{d}, \quad (40)$$

(39) becomes $\mathbf{a}_h + \nu\mathbf{b}_h + \mathbf{C}^T\boldsymbol{\lambda} = \mathbf{0}$. The constraint force $\mathbf{C}^T\boldsymbol{\lambda}$ is unknown, but it can be eliminated as follows. Let \mathbb{P} denote the orthogonal projector onto $\text{Null}(\mathbf{C})$, defined for any vector \mathbf{f} by

$$\mathbb{P}\mathbf{f} = \mathbf{f} - \mathbf{C}^T(\mathbf{C}\mathbf{C}^T)^{-1}\mathbf{C}\mathbf{f}. \quad (41)$$

Applying \mathbb{P} to (39) eliminates the constraint force and gives $\mathbb{P}\mathbf{a}_h + \nu\mathbb{P}\mathbf{b}_h = \mathbf{0}$, an overdetermined system in the single scalar ν . The least-squares solution in the \mathbf{M} -weighted inner product is

$$\nu = -\frac{(\mathbb{P}\mathbf{b}_h)^T \mathbf{M} (\mathbb{P}\mathbf{a}_h)}{(\mathbb{P}\mathbf{b}_h)^T \mathbf{M} (\mathbb{P}\mathbf{b}_h)}. \quad (42)$$

Each projection requires only a sparse triangular solve with a pre-factored $\mathbf{C}\mathbf{C}^T$; no dense null-space basis is formed.

Remark 6.1. Every quantity in (42) (the matrices \mathbf{M} , \mathbf{K} , \mathbf{C} , the convective residual \mathbf{r}_{conv} , and the velocity \mathbf{d} and its time derivative $\dot{\mathbf{d}}$) is computed entirely from the measured velocities and the Q9 shape functions. No boundary conditions, pressure reconstruction, or forward simulation enter the computation.

Interior nodes. At the boundary of the measurement window, the outermost elements have nodes whose basis function support extends to elements that lie outside the field of view. The momentum balance (39) at such a node is incomplete because contributions from the missing elements are absent. We therefore restrict the estimate to *interior* nodes: those whose complete element neighborhood lies within the measurement window. Let \mathcal{I} denote the set of interior DOFs. The divergence constraint is restricted to these DOFs, $\mathbf{C}_{\mathcal{I}} = \mathbf{C}(:, \mathcal{I})$, and the projector (41) and estimate (42) are evaluated on this reduced set with $\mathbf{M}_{\mathcal{I}} = \mathbf{M}(\mathcal{I}, \mathcal{I})$.

Two features of this formulation deserve emphasis. First, the vectors \mathbf{a}_h and \mathbf{b}_h involve at most first spatial derivatives of the measured velocity; no second spatial derivatives are needed, unlike methods based on the strong-form Navier–Stokes equations. Second, the entire identification is a direct algebraic computation: no forward solve, no adjoint, no iterative optimization. The procedure is summarized in Algorithm 1.

6.2 Temporal polynomial regression

Algorithm 1 requires the velocity \mathbf{d} and its time derivative $\dot{\mathbf{d}}$ at the measurement grid points. In a PIV experiment, what is available is a sequence of N velocity snapshots at times t_0, t_1, \dots, t_{N-1} , so both \mathbf{d} and $\dot{\mathbf{d}}$ must be estimated from the discrete time series. A simple finite difference $\dot{\mathbf{d}} \approx (\mathbf{d}^{n+1} - \mathbf{d}^n)/\Delta t$ amplifies measurement noise by a factor $1/\Delta t$, degrading the viscosity estimate.

We address this with a sliding-window polynomial regression, following the Savitzky–Golay approach [28]. Within a window of W consecutive snapshots at times t_0, \dots, t_{W-1} ,

Algorithm 1 Viscosity estimation from velocity field data.

Require: Velocity \mathbf{d} and its time derivative $\dot{\mathbf{d}}$ at grid points

Ensure: Kinematic viscosity ν

- 1: Assign Q9 elements to the measurement grid.
 - 2: Assemble \mathbf{M} , \mathbf{K} , \mathbf{C} on these elements.
 - 3: Identify interior DOFs \mathcal{I} (nodes with complete element support).
 - 4: Restrict: $\mathbf{C}_{\mathcal{I}} \leftarrow \mathbf{C}(:, \mathcal{I})$.
 - 5: Factor $\mathbf{C}_{\mathcal{I}}\mathbf{C}_{\mathcal{I}}^T$ (sparse, once).
 - 6: Compute $\mathbf{a}_h = \mathbf{M}\dot{\mathbf{d}} + \mathbf{r}_{\text{conv}}(\mathbf{d})$ and $\mathbf{b}_h = \mathbf{K}\mathbf{d}$.
 - 7: Restrict to interior DOFs: $\mathbf{a}_{\mathcal{I}} \leftarrow \mathbf{a}_h(\mathcal{I})$, $\mathbf{b}_{\mathcal{I}} \leftarrow \mathbf{b}_h(\mathcal{I})$.
 - 8: Project: $\mathbb{P}\mathbf{a}_{\mathcal{I}} \leftarrow \mathbf{a}_{\mathcal{I}} - \mathbf{C}_{\mathcal{I}}^T(\mathbf{C}_{\mathcal{I}}\mathbf{C}_{\mathcal{I}}^T)^{-1}\mathbf{C}_{\mathcal{I}}\mathbf{a}_{\mathcal{I}}$ (likewise for $\mathbf{b}_{\mathcal{I}}$).
 - 9: $\nu \leftarrow -\frac{(\mathbb{P}\mathbf{b}_{\mathcal{I}})^T\mathbf{M}_{\mathcal{I}}(\mathbb{P}\mathbf{a}_{\mathcal{I}})}{(\mathbb{P}\mathbf{b}_{\mathcal{I}})^T\mathbf{M}_{\mathcal{I}}(\mathbb{P}\mathbf{b}_{\mathcal{I}})}$.
-

a polynomial of degree $p < W$ is fit to each DOF's time series by least squares. The fitted polynomial is then evaluated, along with its time derivative, at the window midpoint $t_{\text{mid}} = (t_0 + t_{W-1})/2$.

The regression weights are independent of the data. Defining the centered Vandermonde matrix $V_{ij} = (t_i - t_{\text{mid}})^j$ and its pseudoinverse $V^+ = (V^T V)^{-1} V^T$, the fitted value and derivative at t_{mid} are

$$d_k(t_{\text{mid}}) = \mathbf{w}_{\text{val}}^T \mathbf{d}_k, \quad \dot{d}_k(t_{\text{mid}}) = \mathbf{w}_{\text{der}}^T \mathbf{d}_k, \quad (43)$$

where $\mathbf{w}_{\text{val}} = V_{0,:}^+$ and $\mathbf{w}_{\text{der}} = V_{1,:}^+$ are the zeroth- and first-order weight vectors, and $\mathbf{d}_k = (d_k(t_0), \dots, d_k(t_{W-1}))^T$ is the vector of samples for DOF k . The weights are computed once and applied to all DOFs by a single matrix–vector product.

When $p < W - 1$, the polynomial fit has $W - p - 1$ residual degrees of freedom that average out noise. The noise in the smoothed velocity and its derivative scales as $\sim \sigma / \sqrt{W - p - 1}$ compared to the raw measurement noise σ . The polynomial degree p controls the bias–variance tradeoff: higher p captures more temporal curvature (relevant for oscillating flows) but leaves fewer degrees of freedom for averaging.

Sliding the window one step at a time through the N snapshots produces $N - W + 1$ viscosity estimates. For noisy data, these are averaged to reduce variance. When multiple independent noise realizations are available (e.g., from different PIV acquisition runs), the procedure is applied to each realization, and the results are pooled.

6.2.1 Pre-filtering of noisy snapshots

Measurement noise violates the incompressibility constraint $\mathbf{C}\mathbf{d} = \mathbf{0}$, introducing a compressible velocity component that biases the viscosity estimate. Before applying the temporal regression, each noisy snapshot is projected onto the divergence-free subspace using $\mathbb{P}\mathbf{d} = \mathbf{d} - \mathbf{C}^T(\mathbf{C}\mathbf{C}^T)^{-1}\mathbf{C}\mathbf{d}$, where the projection uses all DOFs in the measurement window (not just the interior ones). For isotropic noise in two dimensions, this removes roughly 30–50% of the noise variance.

6.3 Numerical demonstration

We demonstrate the method on the backward-facing step (Section 4.2), using its converged velocity field as synthetic PIV data. The backward-facing step at $Re = 100$ ($\nu_{\text{true}} = 0.005$) provides a nearly steady test case: the converged flow changes by $O(10^{-4})$ between consecutive time steps, so the time derivative $\dot{\mathbf{d}}$ is negligible compared to the spatial terms. Nevertheless, we use the full transient formulation with $N = 65$ snapshots separated by $\Delta t = 0.007$.

A rectangular measurement window of 75 elements (498 interior DOFs) is placed just downstream of the step ($x \in [3, 5]$, $y \in [0.3, 0.7]$, Figure 22), capturing the recirculation zone where the velocity gradients, and hence the viscous signal, are strongest. With clean data,

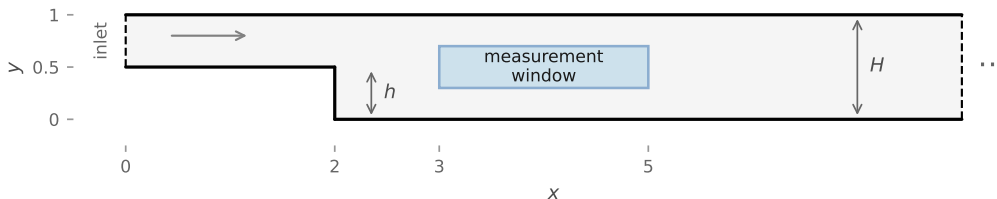


Figure 22: Backward-facing step geometry with the measurement window used for viscosity estimation. The window is placed in the recirculation region downstream of the step, away from all domain boundaries.

the sliding window ($W = 33$, $p = 1$) recovers $\nu_{\text{est}}/\nu_{\text{true}} = 0.9998$ (averaged over all window positions). Four additional windows placed elsewhere in the channel (developed flow, far downstream, outlet region) give comparably accurate results, confirming that the method is not sensitive to the choice of window location provided the velocity gradients are sufficiently strong.

To simulate measurement uncertainty, isotropic Gaussian noise of standard deviation $\sigma = \varepsilon V_{\text{rms}}$ is added to each velocity component, where $V_{\text{rms}} = \sqrt{\langle |\mathbf{v}|^2 \rangle}$ is the spatial root-mean-square velocity. Each noisy snapshot is pre-filtered onto the divergence-free subspace before regression. Figure 23 shows the resulting viscosity estimates as a function of noise level ε . At 1% noise, the method recovers $\nu_{\text{est}}/\nu_{\text{true}} = 0.99 \pm 0.02$ (mean \pm one standard deviation over 20 independent noise realizations and all sliding-window positions).

The dominant noise degradation mechanism is an *errors-in-variables* attenuation bias: the viscous term $\mathbf{b}_h = \mathbf{K}\mathbf{d}$ appears in the denominator of (42), and noise in \mathbf{d} biases it toward zero. This effect can be mitigated by increasing the temporal window size W , which averages the noise over more snapshots. Among the polynomial degrees tested ($p = 1, 2, 3$), $p = 1$ (linear regression) consistently provides the best results because it leaves the most degrees of freedom ($W - 2$) for noise averaging. In a typical PIV experiment with frame rates of hundreds of Hz, windows of $W \geq 30$ frames are easily achievable.

6.4 Discussion

The numerical demonstration shows that the PMPG stationarity condition can be read backwards to recover the kinematic viscosity directly from velocity field data, with near-

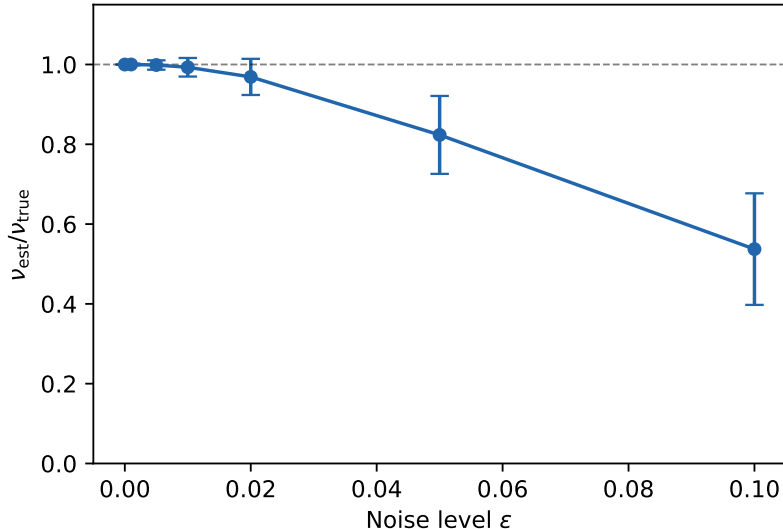


Figure 23: Viscosity estimate vs. noise level for the near-step measurement window ($W = 33$, $p = 1$). Error bars show ± 1 standard deviation over 20 noise realizations. Pre-filtering onto the divergence-free subspace is applied to each noisy snapshot before regression.

exact results on clean data and graceful degradation under measurement noise. The most important practical consideration is the placement of the measurement window: the accuracy depends strongly on the local signal-to-noise ratio of the viscous term $\mathbf{K}\mathbf{d}$, so windows should target regions with strong velocity gradients (shear layers, recirculation zones, boundary layers) where the viscous contribution to the momentum balance is largest relative to measurement noise.

The demonstration above assumed a spatially uniform Newtonian viscosity, but the formulation extends naturally to spatially varying viscosity $\nu(\mathbf{x}) = \sum_a N_a(\mathbf{x}) \nu_a$. The viscous term becomes $\sum_a \nu_a \mathbf{K}_a \mathbf{d}$ with $(K_a)_{ij} = \int_{\Omega} N_a \nabla N_i \cdot \nabla N_j d\Omega$, and the projected system becomes a linear system in the vector $\boldsymbol{\nu} = (\nu_1, \dots, \nu_{n_{\text{nodes}}})^T$. This opens the possibility of mapping the spatial distribution of effective viscosity (including turbulent eddy viscosity) directly from PIV measurements. For generalized Newtonian fluids, where the viscosity depends on the local strain rate, $\nu = \nu(\dot{\gamma})$, the same framework applies: the rheological parameters enter the projected momentum balance algebraically and can be identified without pressure reconstruction or forward simulation.

7 Summary and future work

We have presented the first finite element implementation of the principle of minimum pressure gradient (PMPG) for incompressible viscous flow. Unlike Galerkin formulations, which discretize a weak form of the governing equations, the present approach applies the Rayleigh–Ritz method directly to the PMPG variational principle: at each instant, the nodal velocity rates \mathbf{d} are determined by minimizing the L^2 norm of the implied pressure gradient, subject to incompressibility and boundary constraints. This variational structure has three important

consequences:

1. **Velocity-rate-only formulation.** No pressure finite element space is introduced and no inf-sup condition must be satisfied. Pressure-related quantities enter solely through the Lagrange multipliers of the constraint system, which provide wall forces (pressure and viscous shear) as a direct byproduct of the solve.
2. **Symmetric positive definite system matrix.** Because convection appears only in the explicit right-hand side, the system matrix $\mathbf{M} + \nu\Delta t \mathbf{K}$ is SPD for any positive viscosity and time step, regardless of the Reynolds number. The formulation therefore requires no stabilization, even on coarse meshes in the convection-dominated regime.
3. **Built-in error indicator.** The element-wise PMPG functional density measures the local momentum residual at zero additional cost, providing a natural criterion for adaptive mesh refinement without adjoint problems or reference solutions.

The formulation was verified against two exact solutions: Poiseuille channel flow (machine-precision recovery) and the Kovaszny solution (spatial convergence rate ~ 3.3 , consistent with $O(h^3)$ for biquadratic elements). It was validated against published benchmark data for the lid-driven cavity (Ghia et al. [15]), the backward-facing step (Armaly et al. [16]), and flow past a circular cylinder (Dennis & Chang [17], Tritton [18], Williamson [19]), demonstrating good agreement across a range of Reynolds numbers. In particular, the lid-driven cavity at $Re = 1000$ on coarse wall-graded meshes with element Péclet numbers up to 42 confirmed the oscillation-free behavior predicted by the SPD structure.

The Lagrange multipliers from the saddle-point system were used to extract wall forces without pressure reconstruction, yielding reattachment lengths on the backward-facing step and drag and lift coefficients on the cylinder that agreed with published values to within a few percent.

The error indicator was validated on the Kovaszny problem (Spearman $\rho = 0.996$ correlation with the true element-wise velocity error) and applied to the backward-facing step, where a single round of equidistribution-based adaptation reduced the element count by 19% while maintaining the same functional value.

Beyond forward simulation, we showed that the PMPG stationarity condition can be read backwards to estimate the kinematic viscosity directly from velocity field data. The constraint forces are eliminated by projecting onto the divergence-free subspace, and the viscosity is recovered from a single ratio of inner products, requiring no boundary conditions, pressure reconstruction, or iterative optimization. On a backward-facing step test case, the estimator recovers the true viscosity to within 0.02% from clean data, and to within 1% at 1% measurement noise. The formulation extends naturally to spatially varying and non-Newtonian viscosities.

The present implementation is a first step toward realizing the full potential of the PMPG framework. Several extensions are envisioned:

- **Higher Reynolds numbers.** The cavity results at $Re = 1000$ (Section 4.1.3) show that the PMPG formulation is structurally stable at high element Péclet numbers, producing smooth solutions even when the boundary layer is not resolved by a single

element. At still higher Reynolds numbers, boundary and shear layers become thinner and require finer meshes for *accuracy*. The element-wise PMPG functional density (Section 5) already identifies under-resolved regions, and the adaptive refinement strategy demonstrated on the backward-facing step (Section 5.3) provides a natural mechanism for concentrating elements where they are needed, without requiring any stabilization machinery.

- **Three-dimensional extension.** The formulation extends naturally to 3D using 27-node hexahedral elements (Q27) with trilinear geometry mapping. The divergence constraint remains linear, and the saddle-point structure is unchanged.
- **Turbulence modeling.** The PMPG framework may offer new perspectives on turbulence modeling, as the variational principle provides a natural energy-based criterion for subgrid-scale closures.
- **Moving boundaries and fluid–structure interaction.** The constraint-based architecture is well-suited for incorporating moving boundaries, as the constraints can be updated at each time step without modifying the underlying element formulation. Furthermore, the Lagrange multipliers provide the total nodal forces (pressure and viscous shear) at wall nodes as a direct byproduct of the solve, eliminating the need for separate force reconstruction. These nodal forces are precisely the coupling loads required by a structural solver, making the PMPG formulation a natural candidate for partitioned or monolithic fluid–structure interaction schemes.
- **Connections to the variational framework.** The PMPG principle is part of a broader variational framework for fluid mechanics [9, 6] that includes Gauss’s principle and the Appell function. Exploring these connections may yield new computational strategies and physical insights.

Acknowledgments

The author thanks Professors Haithem Taha and Perry Johnson (Department of Mechanical and Aerospace Engineering, University of California, Irvine) for valuable discussions during the development of this work.

Appendices

A Optimality of the 2×2 Gauss collocation points

This appendix analyzes the choice of collocation points for the divergence-free constraint (24). We introduce a rigorous measure of divergence leakage, derive optimal collocation-point placements in closed form, and explain why the 2×2 Gauss points (which are not per-element optimal) produce the best results in assembled finite element computations. All notation follows the main text; in particular, \mathbf{d} , \mathbf{B}_ξ , \mathbf{B}_η , \mathbf{J} , and $\mathbf{c}_k^{\text{div}}$ are defined in equations (14), (17), (19), and (24).

A.1 Divergence leakage operator

At any point (ξ, η) in the reference element, the scaled divergence $(\nabla \cdot \mathbf{v}) \det(\mathbf{J}) = \mathbf{c}^{\text{div}} \cdot \mathbf{d}$ is a linear function of the element DOF vector $\mathbf{d} \in \mathbb{R}^{18}$. To measure the integrated divergence residual over the element we define the *divergence mass matrix*

$$\mathbf{M}_{\text{div}} = \int_{-1}^1 \int_{-1}^1 (\mathbf{c}^{\text{div}})^T \mathbf{c}^{\text{div}} d\xi d\eta \in \mathbb{R}^{18 \times 18}, \quad (44)$$

which is symmetric positive semi-definite and satisfies $\mathbf{d}^T \mathbf{M}_{\text{div}} \mathbf{d} = \int_{-1}^1 \int_{-1}^1 [(\nabla \mathbf{v}) \det(\mathbf{J})]^2 d\xi d\eta$. For a square element where $\det(\mathbf{J})$ is constant, this is proportional to $\int (\nabla \cdot \mathbf{v})^2 d\Omega$.

Evaluating the constraint (24) at four collocation points yields a 4×18 constraint matrix \mathbf{A} whose null space $\text{Null}(\mathbf{A}) \subset \mathbb{R}^{18}$ has dimension 14. Let $\mathbf{V} \in \mathbb{R}^{18 \times 14}$ be an orthonormal basis for this null space. Every admissible velocity field satisfies $\mathbf{d} = \mathbf{V} \mathbf{z}$ for some $\mathbf{z} \in \mathbb{R}^{14}$, and its divergence residual is

$$\mathbf{d}^T \mathbf{M}_{\text{div}} \mathbf{d} = \mathbf{z}^T \underbrace{\mathbf{V}^T \mathbf{M}_{\text{div}} \mathbf{V}}_{\mathbf{L}} \mathbf{z}, \quad (45)$$

where $\mathbf{L} \in \mathbb{R}^{14 \times 14}$ is the *leakage operator*. Its trace $\text{tr}(\mathbf{L})$ measures the total divergence leakage and admits the basis-free formula

$$\text{tr}(\mathbf{L}) = \text{tr}(\mathbf{M}_{\text{div}}) - \text{tr}(\mathbf{A} \mathbf{M}_{\text{div}} \mathbf{A}^T (\mathbf{A} \mathbf{A}^T)^{-1}). \quad (46)$$

Since the 14 eigenvalues of \mathbf{L} interlace with those of \mathbf{M}_{div} , the leakage satisfies the lower bound

$$\text{tr}(\mathbf{L}) \geq \sum_{i=1}^{14} \mu_i, \quad (47)$$

where $\mu_1 \leq \dots \leq \mu_{18}$ are the eigenvalues of \mathbf{M}_{div} . This bound is the best any four linear constraints can achieve.

A.2 Analysis on the unit square

On the reference square $[-1, 1]^2$, the Jacobian is the identity and $\mathbf{c}^{\text{div}} = (\mathbf{B}_\xi \ \mathbf{B}_\eta)$. The tensor-product structure of the Q9 shape functions allows \mathbf{M}_{div} to be assembled from the 3×3 one-dimensional mass, stiffness, and mixed matrices of the 1D Lagrange basis (13).

The matrix has $\text{rank}(\mathbf{M}_{\text{div}}) = 8$: the 10-dimensional null space consists of the biquadratic velocity fields that are exactly divergence-free. The 8 nonzero eigenvalues, reflecting the D_4 symmetry of the square, are:

$$\begin{aligned} \mu_1 &= \frac{17 - \sqrt{209}}{15} \approx 0.170, & \mu_2 &= \frac{4}{15} \approx 0.267, & \mu_{3,4} &= \frac{27 - \sqrt{409}}{10} \approx 0.678 \quad (\times 2), \\ \mu_5 &= \frac{17 + \sqrt{209}}{15} \approx 2.097, & \mu_6 &= \frac{8}{3} \approx 2.667, & \mu_{7,8} &= \frac{27 + \sqrt{409}}{10} \approx 4.722 \quad (\times 2), \end{aligned} \quad (48)$$

with $\sum_{i=1}^8 \mu_i = 16 = \text{tr}(\mathbf{M}_{\text{div}})$. The theoretical minimum leakage (47) equals the sum of the four smallest nonzero eigenvalues:

$$\text{tr}(\mathbf{L})_{\min} = \frac{34}{5} - \frac{\sqrt{209}}{15} - \frac{\sqrt{409}}{5} \approx 1.791. \quad (49)$$

A.3 Optimal collocation points

The D_4 symmetry of the square constrains the optimal configuration. We consider two natural one-parameter families that respect this symmetry.

Diagonal placement: $(\pm s, \pm s)$. Evaluating (46) symbolically yields a closed-form leakage:

$$\mathcal{L}_{\text{diag}}(s) = \frac{4(9234s^8 - 18684s^6 + 16632s^4 - 6858s^2 + 1297)}{45(3s^4 - 4s^2 + 2)(36s^4 - 48s^2 + 25)}. \quad (50)$$

The minimum occurs at $s^* \approx 0.4959$, with the closed-form value at $s = 1/2$ essentially matching it: $\mathcal{L}_{\text{diag}}(1/2) = 18746/10431 \approx 1.797$. The 2×2 Gauss points correspond to $s = 1/\sqrt{3}$, giving $\mathcal{L}_{\text{diag}}(1/\sqrt{3}) = 1124/585 \approx 1.921$.

Axis placement: $(0, \pm s)$ and $(\pm s, 0)$. The leakage is $\mathcal{L}_{\text{axis}}(s) = (19332s^4 - 45552s^2 + 42352)/(3375s^4 - 9000s^2 + 9000)$, with optimum ≈ 4.564 , more than 2.5 times the theoretical bound. Axis points probe the divergence along the coordinate directions and miss the dominant diagonal stretching modes ($\mu_{7,8} \approx 4.72$).

Table 2 collects the key results.

Table 2: Leakage $\text{tr}(\mathbf{L})$ for four-point collocation schemes on the unit square. The ratio is relative to the theoretical bound (49).

Collocation points	s	$\text{tr}(\mathbf{L})$	Ratio to bound
Theoretical bound (any 4 constraints)	—	1.791	1.000
Optimal diagonal	0.496	1.797	1.003
$(\pm \frac{1}{2}, \pm \frac{1}{2})$	0.500	1.797	1.003
2×2 Gauss	$1/\sqrt{3}$	1.921	1.073
Optimal axis	0.755	4.564	2.548

By the per-element measure, the diagonal $(\pm \frac{1}{2}, \pm \frac{1}{2})$ points are nearly optimal (within 0.3% of the bound), the 2×2 Gauss points are 7.3% above it, and axis points are dramatically inferior.

General quadrilaterals. To verify robustness, the analysis was repeated on 200 random convex quadrilaterals (corner perturbations with standard deviation 0.3). The diagonal $(\pm \frac{1}{2}, \pm \frac{1}{2})$ points maintain a mean leakage ratio of 1.02 and worst case below 1.19; the 2×2 Gauss points give a mean ratio of 1.09. Axis-aligned points exceed a ratio of 2.5 on average.

A.4 Polynomial orthogonality of the 2×2 Gauss rule

Despite their worse per-element leakage, the 2×2 Gauss points produce lower integrated divergence and better velocity convergence in assembled computations (Figure 7). The explanation is a polynomial-degree argument.

In the subparametric formulation, each Jacobian component j_{ij} is at most linear in (ξ, η) ; see (21). The shape function derivatives $\partial N_a/\partial\xi$ are degree (1, 2) and $\partial N_a/\partial\eta$ are degree (2, 1). The products in the divergence constraint (24) therefore satisfy

$$(\nabla \cdot \mathbf{v}) \det(\mathbf{J}) \text{ is at most degree } (2, 2) \text{ in } (\xi, \eta). \quad (51)$$

For any bilinear function $q(\xi, \eta)$ (degree ≤ 1 in each variable), the product $[(\nabla \cdot \mathbf{v}) \det(\mathbf{J})] \cdot q$ is at most degree (3, 3), which the 2×2 Gauss rule integrates exactly. If the divergence constraint vanishes at the four Gauss points, then

$$\int_{\Omega_e} (\nabla \cdot \mathbf{v}) q \, d\Omega = \sum_{k=1}^4 w_k \underbrace{[(\nabla \cdot \mathbf{v}) \det(\mathbf{J})]_{P_k}}_{=0} q(P_k) = 0 \quad \forall q \in Q_1, \quad (52)$$

where $w_k = 1$ are the Gauss weights and the quadrature is exact.

In words: *pointwise collocation at the 2×2 Gauss points implies that the divergence residual is L^2 -orthogonal to the entire bilinear polynomial space $Q_1 = \text{span}\{1, \xi, \eta, \xi\eta\}$ on each element.* The residual divergence can contain only high-order modes (quadratic and above in ξ or η).

Remark A.1. The $(\pm\frac{1}{2}, \pm\frac{1}{2})$ points are not Gauss points for any standard rule. A four-point rule at these locations has insufficient polynomial exactness: the product $[(\nabla \cdot \mathbf{v}) \det(\mathbf{J})] \cdot q$ is degree (3, 3), but four points at $(\pm\frac{1}{2}, \pm\frac{1}{2})$ integrate exactly only up to degree (1, 1). The orthogonality condition (52) therefore does not hold, and the divergence residual retains low-frequency content (including, potentially, a nonzero element-average) that can accumulate coherently across the mesh.

A.5 Consequences for the assembled system

The orthogonality property (52) explains the three features observed in Figure 7:

1. Inter-element cancellation. With the 2×2 Gauss rule, each element's divergence residual is purely high-order: it has zero mean, zero first moments, and zero bilinear moment. High-order residuals oscillate in sign and cancel between neighboring elements whose DOFs are correlated through inter-element continuity. Without this orthogonality, low-frequency residuals (particularly a nonzero element-average divergence) add constructively across the mesh, explaining the higher global divergence produced by the per-element-optimal $(\pm\frac{1}{2}, \pm\frac{1}{2})$ points.

2. Velocity accuracy. By confining the divergence residual to high-order modes, the 2×2 Gauss rule avoids introducing spurious low-order errors into the velocity field. The Lagrange multipliers $\boldsymbol{\lambda}$ in the saddle-point system (26) remain well-determined, and the constrained solution retains the full $O(h^3)$ approximation power of the biquadratic space.

3. Over-constrained schemes. Increasing the number of collocation points (5 or 8 Gauss points) leaves too few unconstrained DOFs for the momentum equation and can degrade performance. The 2×2 rule is the lowest-order Gauss rule that provides the 4 constraints needed to leave $18 - 4 = 14$ DOFs per element, and its polynomial exactness is precisely what is needed for the orthogonality property (52).

A.6 Reconciling per-element and assembled analyses

The single-element leakage analysis and the assembled computations measure different quantities:

- **Per-element leakage** (Sections A.1–A.3) considers the worst-case $\int(\nabla\cdot\mathbf{v})^2 d\Omega$ over *all* velocity fields in $\text{Null}(\mathbf{A})$, on a single isolated element with arbitrary DOFs. By this metric, the $(\pm\frac{1}{2}, \pm\frac{1}{2})$ points are optimal.
- **Assembled divergence** (Figure 7) measures the integrated divergence of the actual numerical solution to a specific PDE, on coupled elements with constraints and momentum enforced simultaneously. By this metric, the 2×2 Gauss rule is superior.

The gap arises because the assembled solution inhabits a highly constrained subspace of the per-element admissible set: inter-element continuity, the momentum equation, and boundary conditions all restrict which velocity fields are realized. Within this restricted space, the polynomial structure of the divergence residual (whether its low-frequency content has been eliminated) matters more than the worst-case amplitude bound. The 2×2 Gauss rule is not the per-element optimum, but it filters the residual in precisely the way that matters for the assembled system.

References

- [1] Alexandre Joel Chorin. Numerical solution of the Navier–Stokes equations. *Mathematics of Computation*, 22(104):745–762, 1968.
- [2] Wang Chang, Francis Giraldo, and Blair Perot. Analysis of an exact fractional step method. *Journal of Computational Physics*, 180(1):183–199, 2002.
- [3] Jean-Luc Guermond, Peter Mineev, and Jie Shen. An overview of projection methods for incompressible flows. *Computer Methods in Applied Mechanics and Engineering*, 195(44–47):6011–6045, 2006.
- [4] Ivo Babuška. The finite element method with Lagrangian multipliers. *Numerische Mathematik*, 20(3):179–192, 1973.
- [5] Franco Brezzi. On the existence, uniqueness and approximation of saddle-point problems arising from Lagrangian multipliers. *Revue française d’automatique, informatique, recherche opérationnelle. Analyse numérique*, 8(R2):129–151, 1974.
- [6] Haithem E. Taha, Cody Gonzalez, and Mohamed Shorbagy. A minimization principle for incompressible fluid mechanics. *Physics of Fluids*, 35(12):123110, 2023.
- [7] Carl Friedrich Gauss. Über ein neues allgemeines Grundgesetz der Mechanik. *Journal für die reine und angewandte Mathematik*, 4:232–235, 1829.
- [8] Paul Appell. Sur une forme générale des équations de la dynamique. *Journal für die reine und angewandte Mathematik*, 121:310–319, 1900.

- [9] Cody Gonzalez and Haithem E. Taha. A variational theory of lift. *Journal of Fluid Mechanics*, 941:A58, 2022.
- [10] Alexander N. Brooks and Thomas J. R. Hughes. Streamline upwind/Petrov–Galerkin formulations for convection dominated flows with particular emphasis on the incompressible Navier–Stokes equations. *Computer Methods in Applied Mechanics and Engineering*, 32(1–3):199–259, 1982.
- [11] Thomas J. R. Hughes, Leopoldo P. Franca, and Marc Balestra. A new finite element formulation for computational fluid dynamics: V. Circumventing the Babuška–Brezzi condition: a stable Petrov–Galerkin formulation of the Stokes problem accommodating equal-order interpolations. *Computer Methods in Applied Mechanics and Engineering*, 59(1):85–99, 1986.
- [12] Philip M. Gresho and Robert L. Sani. *Incompressible Flow and the Finite Element Method*. Wiley, Chichester, 1998.
- [13] Michele Benzi, Gene H. Golub, and Jörg Liesen. Numerical solution of saddle point problems. *Acta Numerica*, 14:1–137, 2005.
- [14] Leslie S. G. Kovasznay. Laminar flow behind a two-dimensional grid. *Mathematical Proceedings of the Cambridge Philosophical Society*, 44(1):58–62, 1948.
- [15] Urmila Ghia, Kirti N. Ghia, and C. T. Shin. High-Re solutions for incompressible flow using the Navier–Stokes equations and a multigrid method. *Journal of Computational Physics*, 48(3):387–411, 1982.
- [16] Bassem F. Armaly, Franz Durst, J. C. F. Pereira, and Bernhard Schönung. Experimental and theoretical investigation of backward-facing step flow. *Journal of Fluid Mechanics*, 127:473–496, 1983.
- [17] S. C. R. Dennis and Gau-Zu Chang. Numerical solutions for steady flow past a circular cylinder at Reynolds numbers up to 100. *Journal of Fluid Mechanics*, 42(3):471–489, 1970.
- [18] David J. Tritton. Experiments on the flow past a circular cylinder at low Reynolds numbers. *Journal of Fluid Mechanics*, 6(4):547–567, 1959.
- [19] C. H. K. Williamson. Vortex dynamics in the cylinder wake. *Annual Review of Fluid Mechanics*, 28:477–539, 1996.
- [20] Ercan Erturk, Thomas C. Corke, and Cihan Gökçöl. Numerical solutions of 2-D steady incompressible driven cavity flow at high Reynolds numbers. *International Journal for Numerical Methods in Fluids*, 48(7):747–774, 2005.
- [21] Mark Ainsworth and J. Tinsley Oden. *A Posteriori Error Estimation in Finite Element Analysis*. Wiley, 2000.

- [22] Rüdiger Verfürth. *A Posteriori Error Estimation Techniques for Finite Element Methods*. Oxford University Press, 2013.
- [23] Christophe Geuzaine and Jean-François Remacle. Gmsh: A 3-D finite element mesh generator with built-in pre- and post-processing facilities. *International Journal for Numerical Methods in Engineering*, 79(11):1309–1331, 2009.
- [24] Maziar Raissi, Paris Perdikaris, and George Em Karniadakis. Physics-informed neural networks: A deep learning framework for solving forward and inverse problems involving nonlinear partial differential equations. *Journal of Computational Physics*, 378:686–707, 2019.
- [25] Maziar Raissi, Alireza Yazdani, and George Em Karniadakis. Hidden fluid mechanics: Learning velocity and pressure fields from flow visualizations. *Science*, 367(6481):1026–1030, 2020.
- [26] Alexandros Kontogiannis, Scott V. Elgersma, Andrew J. Sederman, and Matthew P. Juniper. Learning rheological parameters of non-Newtonian fluids from velocimetry data. *Journal of Fluid Mechanics*, 1011:R3, 2025.
- [27] Fabrice Pierron and Michel Grédias. *The Virtual Fields Method: Extracting Constitutive Mechanical Parameters from Full-field Deformation Measurements*. Springer, New York, 2012.
- [28] Abraham Savitzky and Marcel J. E. Golay. Smoothing and differentiation of data by simplified least squares procedures. *Analytical Chemistry*, 36(8):1627–1639, 1964.